Journal of Computational Physics 229 (2010) 6104–6134

Contents lists available at ScienceDirect

Journal of Computational Physics

journal homepage: www.elsevier.com/locate/jcp

High-order finite-volume methods for the shallow-water equations on the sphere

Paul A. Ullrich [a,*], Christiane Jablonowski [a], Bram van Leer [b]

[a] Department of Atmospheric, Oceanic and Space Sciences, Space Research Building, University of Michigan, 2455 Hayward St., Ann Arbor, MI 48109, United States
[b] Department of Aerospace Engineering, François-Xavier Bagnoud Building, University of Michigan, 1320 Beal Avenue, Ann Arbor, MI 48109, United States

ARTICLE INFO

Article history:
Received 6 October 2009
Received in revised form 16 April 2010
Accepted 27 April 2010
Available online 4 May 2010

Keywords:
High-order
Finite-volume methods
Cubed-sphere
Shallow-water equations
Riemann solvers
Well-balanced schemes

ABSTRACT

This paper presents a third-order and fourth-order finite-volume method for solving the shallow-water equations on a non-orthogonal equiangular cubed-sphere grid. Such a grid is built upon an inflated cube placed inside a sphere and provides an almost uniform grid point distribution. The numerical schemes are based on a high-order variant of the Monotone Upstream-centered Schemes for Conservation Laws (MUSCL) pioneered by van Leer. In each cell the reconstructed left and right states are either obtained via a dimension-split piecewise-parabolic method or a piecewise-cubic reconstruction. The reconstructed states then serve as input to an approximate Riemann solver that determines the numerical fluxes at two Gaussian quadrature points along the cell boundary. The use of multiple quadrature points renders the resulting flux high-order. Three types of approximate Riemann solvers are compared, including the widely used solver of Rusanov, the solver of Roe and the new AUSM$^+$-up solver of Liou that has been designed for low-Mach number flows. Spatial discretizations are paired with either a third-order or fourth-order total-variation-diminishing Runge–Kutta timestepping scheme to match the order of the spatial discretization. The numerical schemes are evaluated with several standard shallow-water test cases that emphasize accuracy and conservation properties. These tests show that the AUSM$^+$-up flux provides the best overall accuracy, followed closely by the Roe solver. The Rusanov flux, with its simplicity, provides significantly larger errors by comparison. A brief discussion on extending the method to arbitrary order-of-accuracy is included.

1. Introduction

Atmospheric models are difficult to engineer, largely due to two factors. Firstly, the flow occurs over the surface of a sphere, rather than in much simpler planar Cartesian geometry and secondly, there are vast scale differences between the large-scale horizontal flow, with length scales that extend to thousands of kilometers, and vertical motions with length scales of about 1–10 km. In addition, the dominant motions in the atmosphere are an example of a low-Mach number regime that is mostly characterized by Mach numbers around $M < 0.4$. Therefore, care must be taken when applying numerical methods from other research fields. In particular, in atmospheric flows high-speed motions are only present in fast atmospheric gravity waves or sound waves. The latter are a solution to the 3D nonhydrostatic equation set, but play a negligible role from a physical viewpoint. Nevertheless, an adequate numerical scheme for atmospheric flows must guarantee stability for fast waves and treat the slow, physically important, motions with high accuracy.

* Corresponding author. Tel.: +1 734 936 5503; fax: +1 734 763 0437.
E-mail addresses: paullric@umich.edu (P.A. Ullrich), cjablono@umich.edu (C. Jablonowski), bram@umich.edu (B. van Leer).

0021-9991/$ - see front matter © 2010 Elsevier Inc. All rights reserved.
doi:10.1016/j.jcp.2010.04.044

A common test bed for atmospheric model development is based on the shallow-water equation set that mimics atmospheric flow in a single layer. A shallow-water model thereby tests the horizontal and temporal discretizations and provides guidance for the numerical schemes suitable for flows with low-Mach numbers. Note that the shallow-water equations do not support sound waves but do capture the fast gravity wave propagation.

There are many numerical schemes that have been tested in shallow-water models on the sphere, all of which have both pros and cons. The spectral transform method discussed in Jakob-Chien et al. [17] achieves high accuracy but tends to exhibit non-physical numerical oscillations near sharp gradients – so-called Gibb's ringing. Spectral transform methods also demand a high computational expense at high resolution that is associated with the computational cost of the Legendre transforms. Finite-difference approaches include those of Heikes and Randall [16] and Ronchi et al. [32]. Hybrid finite-volume methods incorporate both a finite-volume treatment of conservative variables and a finite-difference treatment of momentum and include the models of Lin and Rood [22] and Chen and Xiao [8]. Finite-element type models, including spectral-element (SE) and discontinuous-Galerkin (DG) models have been presented by Taylor et al. [37], Côté and Staniforth [10], Thomas and Loft [39], Giraldo et al. [13] and Nair et al. [26].

The aforementioned models represent a wide variety of computational grids on the sphere such as the latitude–longitude mesh, icosahedral and hexagonal grids, and cubed-spheres meshes. The latter three have become popular over the last decade as they provide an almost regular grid point coverage on the sphere. The uniform distribution of elements avoids the convergence of the meridians that is characteristic for latitude–longitude grids, and thereby alleviates the use of polar filters and other numerical damping techniques. The cubed-sphere grid has also been proven to scale efficiently on massively parallel computing platforms as shown by Taylor et al. [38] and Putman and Lin [30]. These two models are therefore under consideration for operational climate and weather applications at atmospheric modeling centers in the US.

This paper introduces a set of third- and fourth-order-accurate fully-conservative finite-volume methods on cubed-sphere grids and assesses the impact of the high-order accuracy. These finite-volume methods are built upon the reconstruction techniques adopted by the Monotone Upstream-centered Schemes for Conservation Laws (MUSCL) pioneered by Van Leer [44]. Previously, second-order finite-volume methods of this type have been studied for geostropic flows on the sphere by Rossmanith [33], which is based on the flux-difference-splitting technique of LeVeque [20] on a curved manifold.

Fully-conservative finite-volume methods share local conservation properties with spectral-element and discontinuous-Galerkin discretizations, but are potentially more computationally efficient due to their relatively weak Courant–Friedrichs–Lewy (CFL) constraints. Explicit timestepping techniques, when used in combination with these methods, suffer from severe CFL timestep restrictions related to the clustering of nodal points near element edges (which worsens at high-order). On the other hand, finite-volume methods possess a large computational stencil at high-order and so are also potentially difficult to parallelize as effectively as these more compact methods. This difficulty arises primarily in the algorithmic complexity associated with determining which information needs to be communicated between processors. Although DG and SE methods only require information to be communicated between elements and their immediate neighbors, the number of prognotistic quantities associated with each element is significantly larger for these schemes. Whereas for each state variable finite-volume methods store only one value per element, DG and SE methods can, at fourth-order-accuracy, can have up to 10 values per element.

The use of neighboring elements by high-order FV schemes also means that element values must be remapped across coordinate discontinuities, such as those that appear on the cubed-sphere grid. This requirement results in the need for wider ghost regions near coordinate discontinuities on parallel systems in order to accommodate remapping. Schemes with local degrees of freedom, on the other hand, including DG and SE methods, may be more attractive in this regard since remapping is not required, and hence work can be distributed more evenly on parallel architectures.

Although we do not present a technique for constructing a monotone or non-oscillatory scheme in this paper, significant research has been done on this topic for applications in other research areas. For instance, (Weighted) Essentially Non-Oscillatory ((W) ENO)-type reconstructions (e.g. [2,27]), slope limiters (e.g. [43,25]) or flux-corrected transport methods [49] can all be applied to this class of finite-volume methods presented herein. Monotone DG methods, on the other hand, are an active research area.

The method we present involves the use of approximate Riemann solvers to calculate edge fluxes. Most widely used approximate Riemann solvers (such as the solver of Roe [31]) are designed to model flow in the transsonic or supersonic regime rather than in the relatively slow flow regime that is typical for the atmosphere. However, recent advances in the design of approximate Riemann solvers have led to an extension of the Advection Upstream Splitting Method (AUSM, [24]) to low Mach numbers [23]. The use of this new numerical flux formulation, known as AUSM$^+$-up, has so-far been largely limited to the aerospace community. Hence, a test of this new approximate Riemann solver will gauge its applicability for atmospheric models. We also compare the Roe and AUSM$^+$-up schemes to the widely-used and simpler Rusanov solution [19,34,42].

The performance of all schemes will be analyzed via selected standard test cases from the suite of Williamson et al. [46]. Among them are the advection of a cosine bell, steady-state geostrophic flow, steady-state geostrophic flow with compact support, flow over an isolated mountain and the Rossby–Haurwitz wave. In addition, we assess the barotropic instability problem of Galewsky et al. [12] that exhibits sharp vorticity gradients.

The paper is organized as follows: In Section 2 we introduce the cubed-sphere grid with an equiangular projection, which is the underlying grid for all simulations. Section 3 discusses the shallow-water equations in cubed-sphere geometry. The high-order finite-volume framework is described in Section 4. Special attention is paid to a careful discretization of the

topography term. Section 5 gives two examples of finite-volume methods that can be composed under this framework. In particular, the third-order dimension-split piecewise-parabolic method and a fourth-order piecewise-cubic-method are introduced. Section 6 describes the three approximate shallow-water Riemann solvers we will be using in our analysis. The simulation results, discussion and performance assessments are presented in Section 7. Finally, the main findings are summarized in Section 8.

2. The cubed-sphere

We make use of the cubed-sphere grid, which is obtained from projecting a gridded cube onto the surface of the sphere. The cubed-sphere grid has been suggested by Sadourny [35] and Ronchi et al. [32], and has become popular in recent years as an alternative to the classical spherical latitude–longitude mesh. The latter requires special treatment of singularities at the North and South poles due to convergence of the meridians. The cubed-sphere grid instead replaces these two strong singularities with eight weaker singularities that occur at the intersections of three cube faces. These intersections are the corner points of the original cube.

From a mathematical standpoint, the cubed-sphere grid is a tiling of the sphere consisting of six panels that form the faces of a concentric cube projected onto the surface of the sphere. Multiple options exist for the choice of grid on each panel, such as the gnomonic grid, which follows from applying a Cartesian grid to each panel of the cube, or the cubic conformal grid, which maximizes the orthogonality of coordinate vectors (see, for instance, Putman and Lin [29] for a review of the types of cubed-sphere grids). In our model we will make use of the gnomonic (equiangular) cubed-sphere grid, which uses grid lines that have equal central angles relative to the center of the sphere (*i.e.*, this property is also exhibited by equispaced lines of constant longitude). This choice of grid projection leads to elements of similar size, and further leads to coincident grid lines on neighboring panels. A depiction of the cubed-sphere grid and its singularities are given in Fig. 1.

A point on the cubed-sphere in the equiangular projection can be given in terms of equiangular coordinates (α,β,n_p), with $\alpha,\beta \in \left[-\frac{\pi}{4},\frac{\pi}{4}\right]$, or in terms of gnomonic coordinates (X,Y,n_p), with $X,\ Y \in [-1,1]$. In both cases the panel number $n_p \in \{1,2,3,4,5,6\}$. By convention, we choose panels 1–4 to be along the equator, with panels 5 and 6 centered on the northern and southern pole, respectively. One can think of equiangular coordinates as being along the surface of the sphere, whereas gnomonic coordinates are along the surface of the cube. These two coordinate systems are related via

$$X = \tan\alpha, \quad Y = \tan\beta. \tag{1}$$

In this paper we will also make use of the definition

$$\delta = \sqrt{1 + X^2 + Y^2}, \tag{2}$$

which appears frequently in the calculation of metric quantities associated with the cubed-sphere.

The discrete resolution of the cubed-sphere is usually written in the form $N_c \times N_c \times 6$ (in the case of symmetric tiling in the α and β direction), where N_c denotes the number of grid cells in each horizontal direction on a panel. A list of some properties of the cubed-sphere grid is given in Table 1. The table lists the approximate equatorial spacing of grid elements,

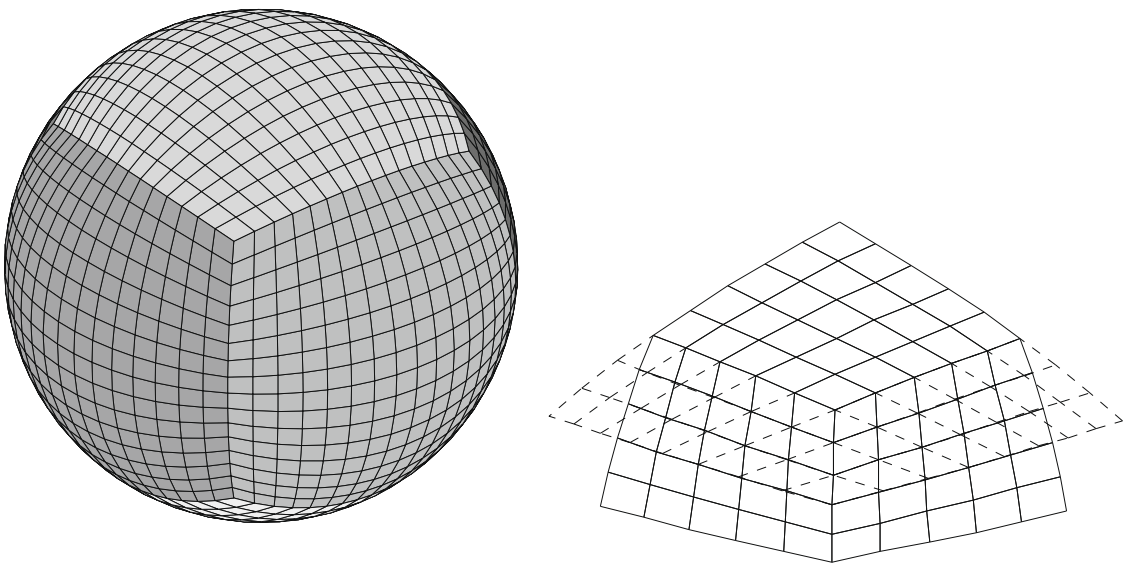

Fig. 1. Left: A 3D view of the tiling of the cubed-sphere, shown here with a 16×16 tiling of elements on each panel. **Right**: A closeup view of the corner of the cubed-sphere, showing the overlap of grid lines from the upper panel ghost cells on the neighboring panels.

Table 1
Properties of the cubed-sphere grid for different resolutions. Here Δx is the grid spacing at the equator, A_{avg} is the average area of all cubed-sphere grid elements, A_{min} is the minimum element area and A_{max} is the maximum element area. RLL_{equiv} denotes the equivalent grid spacing (in degrees) on the regular latitude–longitude grid with the same number of elements and T_{equiv} denotes the approximate triangular truncation of a spectral transform method.

Resolution	Δx (km)	A_{avg} (km^2)	A_{min}/A_{max}	RLL_{equiv}	T_{equiv}
$20 \times 20 \times 6$	500	2.125×10^5	0.7359	5.2°	*T*21
$40 \times 40 \times 6$	250	5.313×10^4	0.7213	2.6°	*T*42
$80 \times 80 \times 6$	125	1.328×10^4	0.7141	1.3°	*T*85
$160 \times 160 \times 6$	62.5	3.321×10^3	0.7106	0.65°	*T*170

average area per element on the sphere, maximum area ratio and equivalent model resolutions of the regular latitude–longitude finite-volume and spectral transform models (under triangular truncation, as argued by Williamson [47]).

3. The shallow-water equations on the cubed-sphere

Under equiangular coordinates, the covariant 2D metric on the cubed-sphere (see, for example, [26]) is given by

$$g_{ij} = \frac{r^2(1+X^2)(1+Y^2)}{\delta^4} \begin{pmatrix} 1+X^2 & -XY \\ -XY & 1+Y^2 \end{pmatrix}, \tag{3}$$

with contravariant inverse

$$g^{ij} = \frac{\delta^2}{r^2(1+X^2)(1+Y^2)} \begin{pmatrix} 1+Y^2 & XY \\ XY & 1+X^2 \end{pmatrix}. \tag{4}$$

The square root of the metric determinant, denoted by $\sqrt{g}$, is then

$$\sqrt{g} = \sqrt{\det(g_{ij})} = \frac{r^2(1+X^2)(1+Y^2)}{\delta^3}. \tag{5}$$

The quantity $\sqrt{g}$ is exactly the Jacobian of the associated coordinate transform, and corresponds to the area of an infinitesmal region $d\alpha \times d\beta$. Without loss of generality we will set the radius of the sphere r to one, which fixes the characteristic length scale to be in terms of Earth radii.

The shallow-water equations in equiangular coordinates can be written as a conservation law of the form (summation over repeated indices is implied)

$$\frac{\partial}{\partial t}\mathbf{q}(\mathbf{x},t) + \frac{1}{\sqrt{g}}\frac{\partial}{\partial x^k}\mathbf{F}^k = \mathbf{\Psi}(\mathbf{q},\mathbf{x}), \tag{6}$$

where $\mathbf{q}$ is the state vector describing the properties of the fluid at each point, $\mathbf{F}^k$ is the flux vector describing the physical response of the flow to gradients in the state vector and $\mathbf{\Psi}$ denotes forcing due to source terms. The state vector $\mathbf{q}$ consists of the height of the fluid, denoted by h, and its horizontal momentum $h\mathbf{u}$, which we can write as a linear combination of the basis vectors along the cubed-sphere as

$$h\mathbf{u} = hu^1\mathbf{g}_1 + hu^2\mathbf{g}_2, \tag{7}$$

where $\mathbf{g}_1$ and $\mathbf{g}_2$ denote the geometric basis vectors in the α and β directions, respectively. Hence, hu^1 and hu^2 can be thought of as the components of the angular momentum along geodesics that are aligned with the grid.[1] The state vector and flux vector then take the form

$$\mathbf{q}(\mathbf{x},t) = \begin{bmatrix} h \\ hu^1 \\ hu^2 \end{bmatrix}, \quad \mathbf{F}^k = \sqrt{g}\begin{bmatrix} U^k \\ \mathcal{T}^{k1} \\ \mathcal{T}^{k2} \end{bmatrix}. \tag{8}$$

The source terms can be written as

$$\mathbf{\Psi} = \begin{bmatrix} 0 \\ \Psi_M^1 + \Psi_C^1 + \Psi_B^1 \\ \Psi_M^2 + \Psi_C^2 + \Psi_B^2 \end{bmatrix}, \tag{9}$$

[1] Note that u^k does not denote exponentiation of u, and should instead be read as "the kth contravariant component of the vector $\mathbf{u}$." Unfortunately, the overloaded nature of this notation may be (understandably) confusing.

where $\mathbf{\Psi}_M$, $\mathbf{\Psi}_C$ and $\mathbf{\Psi}_B$ are 2-component vectors and correspond to the forcing of the momentum terms due to the metric, the Coriolis force and the bottom topography, respectively. Here we have denoted the components of "mass" flux vector by U^k and the "momentum" flux tensor by $\mathcal{T}^{kn}$. In terms of the state vector $\mathbf{q}$ the components of the flux can be written as

$$U^k = hu^k \quad \text{and} \quad \mathcal{T}^{kn} = hu^k u^n + g^{kn}\frac{1}{2}Gh^2, \tag{10}$$

where G denotes the gravitational constant.

In general, the metric source term describes forcing due to the underlying curvature of the coordinate system and, in general curvilinear coordinates, takes the form

$$\mathbf{\Psi}_M^i = -\Gamma^i_{nk}\mathcal{T}^{kn}, \tag{11}$$

where Γ^i_{nk} are the Christoffel symbols of the second kind associated with the metric. In particular, Christoffel symbols can be thought of as terms describing the kth component of the variation of the nth geometric basis vector in the ith direction, and hence can be written as

$$\Gamma^i_{nk} = \frac{\partial \mathbf{g}_n}{\partial x^k}\cdot\mathbf{g}^i. \tag{12}$$

Note that this definition implies that the Christoffel symbols are exactly zero in a Cartesian frame. In component form, the Coriolis source term is given by

$$\mathbf{\Psi}_C^i = -f\mathbf{k}\times h\mathbf{u} = \frac{f}{\sqrt{g}}\begin{bmatrix} g_{12} & g_{22} \\ -g_{11} & -g_{12}\end{bmatrix}\begin{bmatrix} hu^1 \\ hu^2\end{bmatrix}, \tag{13}$$

where $f = 2\Omega\sin\theta$ is the Coriolis parameter in terms of the angular velocity of the Earth Ω and the latitude θ. Finally, the source terms due to varying bottom topography (denoted by z) can be written as

$$\mathbf{\Psi}_B^i = -Gh\nabla^i z = -Ghg^{ij}\frac{\partial z}{\partial x^j}. \tag{14}$$

Given the metric (3) associated with the equiangular cubed-sphere, the metric source term can be written as

$$\mathbf{\Psi}_M = \frac{2}{\delta^2}\begin{bmatrix} -XY^2 hu^1u^1 + Y(1+Y^2)hu^1u^2 \\ X(1+X^2)hu^1u^2 - X^2Yhu^2u^2\end{bmatrix}. \tag{15}$$

Note that in the special case of equiangular coordinates we have that $\Gamma^i_{kn}g^{kn} = 0$, which removes any dependence of the metric source term on the gravitational term $\frac{1}{2}Gh^2$. The Coriolis source term differs depending on whether the underlying panel is equatorial or polar, since

$$\sin\theta = \begin{cases} \frac{Y}{\delta} & \text{if } n_p \in \{1,2,3,4\}, \\ \frac{p}{\delta} & \text{if } n_p \in \{5,6\},\end{cases} \tag{16}$$

where p is a panel indicator given by, for instance,

$$p = \text{sign}(\theta) = \begin{cases} 1 & \text{on the northern panel } (n_p = 5), \\ -1 & \text{on the southern panel } (n_p = 6).\end{cases} \tag{17}$$

Hence, for equatorial panels, we have

$$\mathbf{\Psi}_{C,eq.} = \frac{2\Omega}{\delta^2}\begin{bmatrix} -XY^2 & Y(1+Y^2) \\ -Y(1+X^2) & XY^2\end{bmatrix}\begin{bmatrix} hu^1 \\ hu^2\end{bmatrix}. \tag{18}$$

And for polar panels, we have

$$\mathbf{\Psi}_{C,pol.} = \frac{2p\Omega}{\delta^2}\begin{bmatrix} -XY & (1+Y^2) \\ -(1+X^2) & XY\end{bmatrix}\begin{bmatrix} hu^1 \\ hu^2\end{bmatrix}. \tag{19}$$

4. The high-order finite-volume approach

In this section we present the high-order finite-volume approach we use as a framework for solving the shallow-water equations in cubed-sphere geometry.

4.1. Overview

In the full finite-volume approach we first integrate the shallow-water conservation laws in the form (6) over a given element $\mathcal{Z}$ (with area $|\mathcal{Z}|$) and make use of Gauss' divergence theorem to write the flux term as an integral around the boundary $\partial\mathcal{Z}$, giving

$$\frac{\partial}{\partial t}\bar{\mathbf{q}} + \frac{1}{|\mathcal{Z}|}\oint_{\partial\mathcal{Z}} \mathbf{F}^k(\bar{\mathbf{q}})\, d\ell = \overline{\mathbf{\Psi}}, \tag{20}$$

where the integration is along the line segment $d\ell$ and the overline denotes an average of the form

$$\bar{\phi} = \frac{1}{|\mathcal{Z}|}\int_{\mathcal{Z}} \phi\, dV, \tag{21}$$

where $dV = \sqrt{g}\, d\alpha\, d\beta$ denotes the infinitesmal volume element. Note that the volume-averaged formulation (20) is exactly equivalent to the original shallow-water equations, and it is left to us to define an appropriate discretization over each of the terms in this expression.

In this paper we will only consider discretizations where each panel consists of a regular rectangular arrangement of elements of dimension $N_c \times N_c$. The angle subtended by an element is then defined by

$$\Delta = \frac{1}{N_c}\frac{\pi}{2}. \tag{22}$$

Hence, for each cubed-sphere panel with equiangular coordinate axes (α,β) and equiangular element arrangement, we can define

$$\alpha_i = -\frac{\pi}{4} + \left(i - \frac{1}{2}\right)\Delta \quad \text{and} \quad \beta_j = -\frac{\pi}{4} + \left(j - \frac{1}{2}\right)\Delta, \tag{23}$$

where full indices $i, j = 1,\ldots,N_c$ are used to denote element center-points and half-indices $i,j = (\frac{1}{2}, \frac{3}{2}, \ldots, N_c + \frac{1}{2})$ are used to denote element edges. Hence, the region in (α,β)-space occupied by the element (i,j) is defined by

$$\mathcal{Z}_{ij} = \left[\alpha_{i-1/2}, \alpha_{i+1/2}\right] \times \left[\beta_{j-1/2}, \beta_{j+1/2}\right]. \tag{24}$$

4.2. Orthonormalization and the orthonormal Riemann problem

The schemes discussed in this paper all transform the reconstructed velocity field at element edges into an orthonormal frame consisting of velocity components perpendicular and parallel to the element edge (here denoted by u and v). This approach significantly reduces the complexity of the problem since we only need to solve orthonormal Riemann problems (see Section 6) in order to obtain the corresponding fluxes across each interface. In particular, this approach allows us to sidestep problems due to the discontinuity of the coordinate system at panel edges, since the Riemann problem is solved in a single consistent reference frame. Orthonormalization is performed via multiplication with an *orthonormalization matrix* at each point (see, for instance, [5]),

$$\begin{bmatrix} u \\ v \end{bmatrix} = \mathcal{O}(X,Y)\begin{bmatrix} u^1 \\ u^2 \end{bmatrix}, \tag{25}$$

where $\mathcal{O}$ also depends on the type of edge. In general, for translating velocity components along lines of constant α and constant β we have

$$\mathcal{O}^1 = \begin{bmatrix} \frac{1}{\sqrt{g^{11}}} & 0 \\ \frac{g_{12}}{\sqrt{g_{22}}} & \sqrt{g_{22}} \end{bmatrix} \quad \text{and} \quad \mathcal{O}^2 = \begin{bmatrix} 0 & \frac{1}{\sqrt{g^{22}}} \\ \sqrt{g_{11}} & \frac{g_{12}}{\sqrt{g_{11}}} \end{bmatrix}. \tag{26}$$

Using the metric for equiangular cubed-sphere coordinates, we have for grid lines of constant α that the orthonormalization matrix is

$$\mathcal{O}^1 = \begin{bmatrix} \frac{\sqrt{1+X^2}}{\delta} & 0 \\ \frac{-XY\sqrt{1+X^2}}{\delta^2} & \frac{(1+Y^2)\sqrt{1+X^2}}{\delta^2} \end{bmatrix}, \tag{27}$$

and for grid lines of constant β we have

$$\mathcal{O}^2 = \begin{bmatrix} 0 & \frac{\sqrt{1+Y^2}}{\delta} \\ \frac{(1+X^2)\sqrt{1+Y^2}}{\delta^2} & \frac{-XY\sqrt{1+Y^2}}{\delta^2} \end{bmatrix}. \tag{28}$$

Similarly, to obtain the components of the momentum flux in the equiangular cubed-sphere basis we apply a *deorthonormalization matrix* at each point, which is simply the inverse of the corresponding orthonormalization matrix.

In orthonormal form, the source-free shallow-water equations are given by

$$\frac{\partial h}{\partial t}+\frac{\partial}{\partial x}(hu)+\frac{\partial}{\partial y}(hv)=0, \tag{29}$$

$$\frac{\partial (hu)}{\partial t}+\frac{\partial}{\partial x}\left(hu^2+\frac{1}{2}Gh^2\right)+\frac{\partial}{\partial y}(huv)=0, \tag{30}$$

$$\frac{\partial (hv)}{\partial t}+\frac{\partial}{\partial x}(huv)+\frac{\partial}{\partial y}\left(hv^2+\frac{1}{2}Gh^2\right)=0, \tag{31}$$

where x and y denote components of the coordinate vector within the orthonormal frame and u and v are the corresponding velocities.

4.3. Discretization of the metric and Coriolis terms

To discretize the metric and Coriolis terms, we make use of Gaussian quadrature in 2D to evaluate the integral. For a second-order scheme, this requires the evaluation of these source terms at one point within each element – namely, at the element center-point (see Fig. 2). For a fourth-order scheme, we can obtain fourth-order accuracy by evaluating the source terms at four points within each element – in particular, for an element defined on the region $[\alpha_1,\alpha_2]\times[\beta_1,\beta_2]$, at

$$(\alpha,\beta)=\left(\frac{\alpha_1+\alpha_2}{2}\pm\frac{\alpha_2-\alpha_1}{2\sqrt{3}},\frac{\beta_1+\beta_2}{2}\pm\frac{\beta_2-\beta_1}{2\sqrt{3}}\right). \tag{32}$$

For Gaussian quadrature up to fourth-order, all points contribute equally to the integral.

4.4. Discretization of the topography term

Before making a choice of discretization for the underlying topography (denoted by $z(\alpha,\beta,n_p)$), we must consider the important equilibrium case of stationary flow. In this case we have $\mathbf{u}^i=0$ with constant total height $H=h+z$ everywhere, which physically is an equilibrium solution that should be maintained indefinitely. Not all discretizations will automatically retain this property, however those that do are referred to as *well-balanced* schemes (or, alternatively, schemes that preserve the C-property, *e.g.* see [27] or [8]). It is a well-known fact that discretizations that are not well-balanced may introduce spurious oscillations into the flow that are especially evident for states near this equilibrium solution. In order to develop our topography discretization, we begin with the topography source in the form,

$$\mathbf{\Psi}_B=-Gh\nabla z, \tag{33}$$

and observe that it can be rewritten as

$$\mathbf{\Psi}_B=-Gh\nabla H+\nabla\left(\frac{1}{2}Gh^2\right). \tag{34}$$

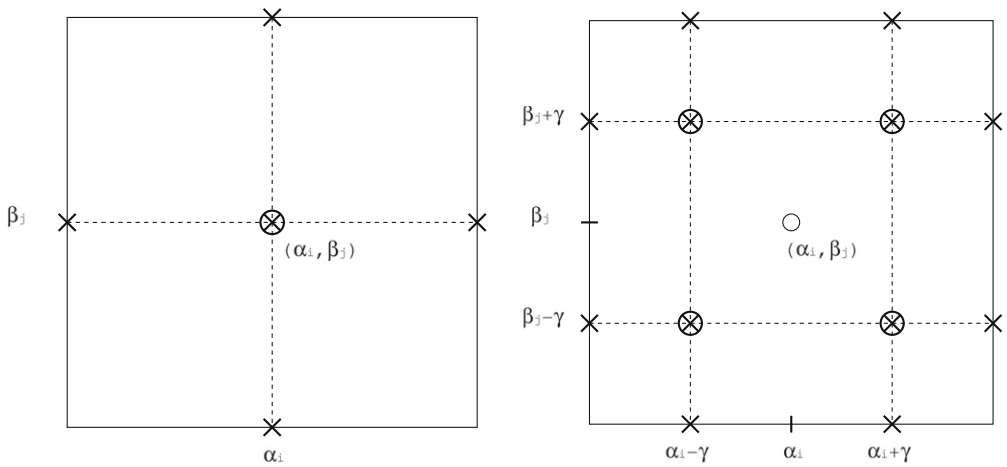

Fig. 2. Gaussian quadrature points used for a first- or second-order finite-volume scheme (left) and for a third- and fourth-order finite-volume scheme (right). Edge points used for calculating fluxes through the boundary are depicted as uncircled $\times$'s. Interior quadrature points are depicted as circled $\times$'s. Here γ is chosen so that the Gaussian quadrature is fourth-order accurate in the size of the grid.

We note that for $\mathbf{u} = 0$ the flux-form momentum equations from (6)–(16) take the form of a balance law,

$$\langle \text{Flux Terms} \rangle = \underbrace{-G \int_{\mathcal{Z}} h \nabla H \, dV}_{(a)} + \underbrace{\int_{\mathcal{Z}} \nabla \left(\frac{1}{2} G h^2 \right) dV}_{(b)}. \tag{35}$$

The benefit of writing the topography source in the form (34) is now revealed; namely, if we can guarantee that $\nabla H = 0$ when H is constant and calculate (35.*b*) in a manner identical to the calculation of the flux, then our discretization will satisfy the well-balanced property.

We observe that this choice of discretization is, in general, non-zero even when no bottom topography is present ($z = 0$). This observation follows from the fact that in the discrete case, the left-hand-side flux term is non-zero when calculated on the manifold (even over a constant field) since we cannot boast the symmetry properties present in purely Cartesian coordinates. Without this additional correction, the model would be unable to maintain a constant height field h with zero flow velocity $\mathbf{u} = 0$, since in discrete form the contour integral would not be exactly zero.

Our choice of discretization of the first term of (34) for the third- and fourth-order schemes is based on using only the evaluated state vector at the Gauss points given in Fig. 2. This choice has the twofold benefit of only requiring the user-specified topography to be given at each Gauss point, and further enforces consistency of the discretization with the second term of (34), which is obtained from the Gauss points along each edge.

Our scheme follows an approach similar to that of Noelle et al. [27]. To begin, we write the first term of (34) in the form

$$-Gh\nabla H = -G \begin{bmatrix} h g^{11} \frac{\partial H}{\partial \alpha} \\ h g^{21} \frac{\partial H}{\partial \alpha} \end{bmatrix} - G \begin{bmatrix} h g^{12} \frac{\partial H}{\partial \beta} \\ h g^{22} \frac{\partial H}{\partial \beta} \end{bmatrix}. \tag{36}$$

Integrating this expression term-by-term gives

$$\int_{\mathcal{Z}} -Gh\nabla H \, dV = -G \begin{bmatrix} \int_{\mathcal{Z}} p^{11} \frac{\partial H}{\partial \alpha} \, d\alpha \, d\beta \\ \int_{\mathcal{Z}} p^{21} \frac{\partial H}{\partial \alpha} \, d\alpha \, d\beta \end{bmatrix} - G \begin{bmatrix} \int_{\mathcal{Z}} p^{12} \frac{\partial H}{\partial \beta} \, d\alpha \, d\beta \\ \int_{\mathcal{Z}} p^{22} \frac{\partial H}{\partial \beta} \, d\alpha \, d\beta \end{bmatrix}, \tag{37}$$

where we have defined

$$p^{ij} = h g^{ij} \sqrt{g} = \frac{h}{\delta} \begin{bmatrix} 1 + Y^2 & XY \\ XY & 1 + X^2 \end{bmatrix}. \tag{38}$$

Without loss of generality, we consider an approach for discretizing an expansion of the form

$$\int_{\mathcal{Z}} p \frac{\partial H}{\partial \alpha} \, d\alpha \, d\beta, \tag{39}$$

observing that this form closely matches that of each of the topography terms in (37). We will make use of the Gauss points given by $(\alpha_i \pm \Delta/2, \beta_j \pm \gamma)$ and $(\alpha_i \pm \gamma, \beta_j \pm \gamma)$ so that the usual Gaussian quadrature can be performed in the β direction. We now require a $O(\Delta^4)$ discretization of the integral in the α direction, which we now construct from two $O(\Delta^2)$ discretizations. Consider centered discretizations of (39) given by

$$\int p \frac{\partial H}{\partial \alpha} \, d\alpha \approx \left(\frac{p_{-\Delta/2} + p_{\Delta/2}}{2} \right) (H_{\Delta/2} - H_{-\Delta/2}) + O(\Delta^2), \tag{40}$$

and

$$\int p \frac{\partial H}{\partial \alpha} \, d\alpha \approx \left(\frac{p_{-\Delta/2} + p_{-\gamma}}{2} \right) (H_{-\gamma} - H_{-\Delta/2}) + \left(\frac{p_{\gamma} + p_{-\gamma}}{2} \right) (H_{\gamma} - H_{-\gamma}) + \left(\frac{p_{\Delta/2} + p_{\gamma}}{2} \right) (H_{\Delta/2} - H_{\gamma}) + O(\Delta^2). \tag{41}$$

Here the subscripts $\pm\Delta/2$ and $\pm\gamma$ denote evaluation of these quantities at $(x_i \pm \Delta/2)$ and $(x_i \pm \gamma)$. Now, for any γ that is a linear function of Δ (except, of course, $\gamma = \pm\Delta/2$) there exists coefficients A_1 and A_2 so that

$$\int_X p \frac{\partial H}{\partial X} dX = A_1 \; [Eq.(40)] + A_2 \; [Eq.(41)] + O(\Delta^4), \tag{42}$$

and, in particular, for $\gamma = \Delta/(2\sqrt{3})$ we obtain a fourth-order accurate approximation with

$$A_1 = \frac{\sqrt{3} - 3}{\sqrt{3} + 3} \quad \text{and} \quad A_2 = \frac{6}{\sqrt{3} + 3}. \tag{43}$$

4.5. The sub-grid-scale reconstruction

All of the numerical approaches discussed in this paper make use of a high-order polynomial sub-grid-scale reconstruction to evaluate the underlying state variables. The order of the sub-grid-scale reconstruction then determines the underlying order of the scheme, when combined with a sufficiently high-order integration scheme for the boundary and the interior.

For a general order-n finite-volume method on the cubed-sphere, we define a sub-grid-scale reconstruction (an approximation to the exact field q, here denoted by $\tilde{q}$) of the form

$$\tilde{q}(\alpha,\beta) = \bar{q} + \sum_{s+t<n} \left[(\alpha-\alpha_0)^s(\beta-\beta_0)^t - a^{(s,t)}\right]\left(\frac{1}{s!t!}\frac{\delta^n q}{\delta\alpha^s\delta\beta^t}\right)_0, \tag{44}$$

where (α_0,β_0) is the element centroid and the $a^{(s,t)}$ are a family of constants defined so that

$$\int_{\mathcal{Z}} \left[(\alpha-\alpha_0)^s(\beta-\beta_0)^t - a^{(s,t)}\right] dV = 0. \tag{45}$$

Here we have made use of s and t to denote terms containing s derivatives in α and t derivatives in β. Further, the discrete approximations to the derivatives of q are denoted with δ instead of ∂ so as to distinguish them from the exact operators; the subscript 0 further denotes evaluation at the element centroid (α_0,β_0). The reconstruction (44) and (45) is chosen so as to preserve the element average, *i.e.*

$$\frac{1}{|\mathcal{Z}|}\int_{\mathcal{Z}} q\, dV = \bar{q}. \tag{46}$$

In order to achieve order-n accuracy with the reconstruction (44), we also require that

$$\left(\frac{1}{s!t!}\frac{\delta^n q}{\delta\alpha^s\delta\beta^t}\right)_0 = \frac{1}{s!t!}\frac{\partial^n q}{\partial\alpha^s\partial\beta^t} + O(\Delta^{n-s-t}). \tag{47}$$

For instance, this restriction requires that for a third-order scheme all first derivative terms must be at least $\sim O(\Delta^2)$, and all second-derivative terms be at least $\sim O(\Delta)$.

Notes.

1. In general, an order-n sub-grid-scale reconstruction will yield an order-n scheme when combined with a flux integral (taken around the boundary of each element) of order n and an interior integration procedure (for source terms) of order $n-1$. Thus, one could potentially sacrifice an order of accuracy for evaluating the source terms and still obtain an order-n scheme. In fact, experiments involving the methods described in this paper have shown that a reduction in the order of the metric and Coriolis source terms has little discernable impact on the results of each simulation since the error in these schemes is primarily dominated by the flux terms.
2. Reconstruction-based schemes have the beneficial property of being, in general, Riemann solver agnostic. That is, in order to solve for the edge fluxes we can make use of any approximate Riemann solver that takes as input a left state $\mathbf{q}_L$ and a right state $\mathbf{q}_R$ as input.

4.6. Treatment of panel edges

The edges of each panel of the cubed-sphere require special consideration, since they represent discontinuities in the coordinate system. There are two instances where data must be communicated across panel edges: first, we require this information to calculate the reconstructed derivatives in elements near panel edges, and second, we require this information when computing fluxes across these interfaces. For the latter case, fluxes computed across panel interfaces are handled no differently than interfaces within panels, since the orthonormalization procedure rewrites the velocities in terms of a local coordinate system that is valid regardless of the panel. Note that this technique differs from that of [33], where fluxes are instead calculated on each panel independently, with the obvious shortfall being that there is no guarantee of mass conservation along panel edges.

In order to provide boundary information to the reconstruction calculation, our choice of boundary conditions can have significant influence on the numerical method. We consider two possible approaches for handling remapping of information across panel boundaries:

- Under the first approach, we interpolate a 1D polynomial parallel to the panel boundary (either through cell centers of elements on the source panel, or using element-averages). This approach is known as *cascade interpolation*, made possible by a previously identified feature of the equiangular coordinate system; namely that grid lines parallel to panel edges are shared by both coordinate systems (see Fig. 1). Unfortunately, this approach is at most second-order accurate since any 1D interpolated polynomial does not take into account the variation perpendicular to the edge.
- Under the second approach, we compute one-sided approximations of the derivatives within each boundary element. Then, by applying four-point Gaussian quadrature within each destination element we approximate the element average in the neighboring panel's ghost elements. A detailed description of this method is given in Appendix A.

In CFD lore, it is generally believed that an n-order accurate numerical method with $(n-1)$-order boundary conditions will still be n-order accurate. However, the strong coupling of the interior cubed-sphere panel boundaries to the numerical

solution does not give us this grace. We have witnessed in several tests that a third-order interior scheme, when combined with a second-order boundary scheme (in this case, a cubic cascade approach), will lead to purely second-order performance in convergence tests. Based on this conclusion, we will make use of the second approach for all of our third- and fourth-order schemes.

As an aside, we note that we must also transform the vector velocities between the panel-specific coordinate systems when performing remapping. This adjustment is achieved by simply applying a transformation matrix in the interpolation step (hence, for each ghost cell the transformation matrix must be applied once for a second-order scheme and four times for a third- or fourth-order scheme).

4.7. Extensions to arbitrary order-of-accuracy

The framework for finite-volume methods presented in this section can be easily extended to arbitrarily large order-of-accuracy, however for every increase in the order-of-accuracy, the finite-volume approach requires a corresponding increase in the size of the stencil. Besides ensuring that the reconstruction is sufficiently accurate, one must also ensure that the flux calculation and source terms are handled appropriately.

In order to ensure that flux calculations are at least nth order accurate, we must solve Riemann problems at $\lceil n/2 \rceil$ points per edge. Similarly, source terms must be evaluated at $\lceil n/2 \rceil^2$ interior points.

5. Numerical approaches

Using the general framework presented in Section 4, we construct two schemes for the shallow-water equations on the sphere. The first scheme is a dimension-split piecewise-parabolic method (FV3s) that is formally second-order accurate, but leads to a method which behaves with third-order accuracy on smooth problems. The second scheme we consider is a fourth-order piecewise-cubic method (FV4).

5.1. A dimension-split piecewise-parabolic scheme (FV3s)

Dimension-split techniques which do not make use of cross-derivatives are formally limited to be no more than second-order accurate. In many cases however, one finds that the error introduced due to neglecting the cross-derivatives is approximately negated when using a symmetric approach. Since dimension-split schemes can be efficiently parallelized, we consider here one such dimension-split approach that combines a formally second-order reconstruction (because cross-derivatives are suppressed) with higher-order approaches for the flux, source terms and panel boundaries.

This method differs from the well-known piecewise-parabolic method of [9] since it uses an inherently discontinuous reconstruction, does not explicitly limit the reconstructed derivatives and uses two Gaussian quadrature points along each edge in order to achieve high-order accuracy in the flux estimates.

In our approach, the discrete derivatives are calculated in equiangular coordinates via

$$\left(\frac{\delta q}{\delta \alpha}\right)_{i,j} = \frac{-\bar{q}_{i+2,j} + 8\bar{q}_{i+1,j} - 8\bar{q}_{i-1,j} + \bar{q}_{i-2,j}}{12\Delta}, \tag{48}$$

$$\left(\frac{\delta q}{\delta \beta}\right)_{i,j} = \frac{-\bar{q}_{i,j+2} + 8\bar{q}_{i,j+1} - 8\bar{q}_{i,j-1} + \bar{q}_{i,j-2}}{12\Delta}, \tag{49}$$

$$\left(\frac{\delta^2 q}{\delta \alpha^2}\right)_{i,j} = \frac{-\bar{q}_{i+2,j} + 16\bar{q}_{i+1,j} - 30\bar{q}_{i,j} + 16\bar{q}_{i-1,j} - \bar{q}_{i-2,j}}{12\Delta^2}, \tag{50}$$

$$\left(\frac{\delta^2 q}{\delta \beta^2}\right)_{i,j} = \frac{-\bar{q}_{i,j+2} + 16\bar{q}_{i,j+1} - 30\bar{q}_{i,j} + 16\bar{q}_{i,j-1} - \bar{q}_{i,j-2}}{12\Delta^2}. \tag{51}$$

Using this form of the reconstructed derivatives all derivative terms are formally $O(\Delta^2)$, since element-averages only represent a $O(\Delta^2)$ approximation to the centroid value. Nonetheless, this scheme would be formally third-order accurate if the cross-derivative $\delta^2 q/\delta\alpha\delta\beta$ was included in the reconstruction. The stencil used by this scheme is depicted in Fig. 3.

In order to preserve stability and high-order accuracy in time, we also make use of the total-variation-diminishing (TVD) third-order Runge–Kutta (RK3) timestepping scheme (see, for example, [14]). For a given semi-discretization with right-hand-side $\mathbf{L}(\mathbf{q})$, this scheme can be written as

$$\begin{aligned}
\mathbf{q}^{(1)} &= \mathbf{q}^n + \Delta t \mathbf{L}(\mathbf{q}^n), \\
\mathbf{q}^{(2)} &= \frac{3}{4}\mathbf{q}^n + \frac{1}{4}\mathbf{q}^{(1)} + \frac{1}{4}\Delta t \mathbf{L}(\mathbf{q}^{(1)}), \\
\mathbf{q}^{n+1} &= \frac{1}{3}\mathbf{q}^n + \frac{2}{3}\mathbf{q}^{(2)} + \frac{2}{3}\Delta t \mathbf{L}(\mathbf{q}^{(2)}).
\end{aligned} \tag{52}$$

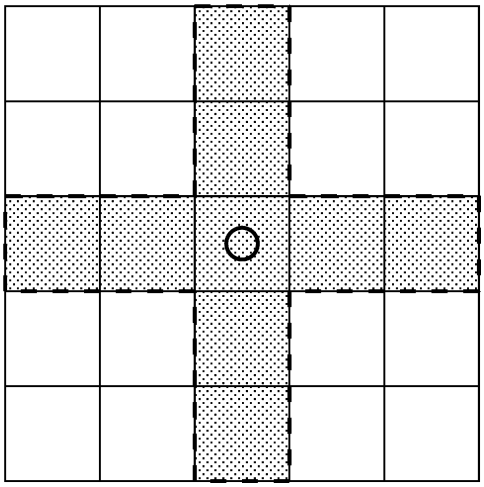

Fig. 3. The stencil for the dimension-split FV3s scheme.

We make use of the CFL number in the form

$$\mathrm{CFL} = \frac{\Delta t}{4|\mathcal{Z}|} \oint_{\partial \mathcal{Z}} |\lambda|_{max}\, ds, \tag{53}$$

where the contour integral is taken around the outside of the element $\mathcal{Z}$ and $|\lambda|_{max}$ denotes the maximum value of the absolute gravity wave speed. Under this definition, the maximum CFL number for the FV3s scheme can be empirically determined to be $\sim$1.05. The maximum CFL number is strongly dependent on the choice of timestepping scheme; if we discretize FV3s with a RK4 timestep scheme, the CFL limit for this scheme increases to $\sim$1.30.

5.2. The piecewise-cubic (FV4) scheme

Our fourth-order finite-volume scheme makes use of a piecewise-cubic sub-grid-scale reconstruction. We first make use of a convolution operator to obtain point values at the center-point of each element. Using these point values, we can then apply a set of standard finite difference operators in order to obtain approximations to the derivatives at the center-points of each element.

Note that the scheme described in this section requires three ghost-elements, which will lead to an increase in parallel communication over the FV3s scheme, for instance. A more efficient fourth-order method (in terms of parallel computational) can be formulated using a 5×5 stencil, but such a decrease in stencil size will also lead to a reduction in computational accuracy. By comparison, the resulting method would only require two ghost cells.

Following the approach of [6] element-averages of a scalar field $\bar{q}$ and the corresponding point-values at element centers q_0 can be interchanged via the formula

$$\bar{q} = q_0 + \frac{\Delta^4}{12|\mathcal{Z}|}\left[\left(\frac{\delta q}{\delta \alpha}\right)_0 \left(\frac{\partial \sqrt{g}}{\partial \alpha}\right)_0 + \left(\frac{\delta q}{\delta \beta}\right)_0 \left(\frac{\partial \sqrt{g}}{\partial \beta}\right)_0\right] + \frac{\Delta^2}{24}\left[\left(\frac{\delta^2 q}{\delta \alpha^2}\right)_0 + \left(\frac{\delta^2 q}{\delta \beta^2}\right)_0\right] + O(\Delta^4). \tag{54}$$

In order to obtain $O(\Delta^4)$ accuracy via this formula, the first and second derivatives in this expression must be approximated to $O(\Delta^2)$, and so can be obtained from

$$\left(\frac{\delta q}{\delta \alpha}\right)_0 = \frac{\bar{q}_{i+1,j} - \bar{q}_{i-1,j}}{2\Delta} + O(\Delta^2),$$
$$\left(\frac{\delta^2 q}{\delta \alpha^2}\right)_0 = \frac{\bar{q}_{i+1,j} - 2\bar{q}_{i,j} + \bar{q}_{i-1,j}}{\Delta^2} + O(\Delta^2),$$

and similarly in the β-direction. The derivatives of the metric terms that appear in (54) can be computed analytically at the element center-points from (5).

Using the point-values obtained from (54) we then apply a standard set of 5-point finite-difference operators in order to approximate derivatives at the center-point. With this technique we obtain sufficiently accurate approximations to the derivatives to support a fourth-order scheme. The stencil obtained from this approach is depicted in Fig. 4.

In order to preserve stability and high-order accuracy in time, we combine our spatial discretization with a fourth-order Runge–Kutta (RK4) timestepping scheme of the form

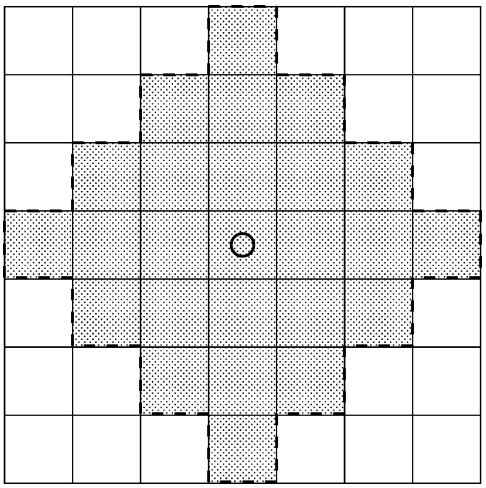

Fig. 4. The reconstruction stencil for the FV4 scheme.

$$\begin{aligned}
\mathbf{q}^{(1)} &= \mathbf{q}^n + \frac{1}{2}\Delta t \mathbf{L}(\mathbf{q}^n), \\
\mathbf{q}^{(2)} &= \mathbf{q}^n + \frac{1}{2}\Delta t \mathbf{L}(\mathbf{q}^{(1)}), \\
\mathbf{q}^{(3)} &= \mathbf{q}^n + \Delta t \mathbf{L}(\mathbf{q}^{(2)}), \\
\mathbf{q}^{n+1} &= -\frac{1}{3}\mathbf{q}^n + \frac{1}{3}\mathbf{q}^{(1)} + \frac{2}{3}\mathbf{q}^{(2)} + \frac{1}{3}\mathbf{q}^{(3)}.
\end{aligned} \tag{55}$$

Using this choice of timestep scheme, the maximum CFL number for the FV4 scheme can be empirically determined to be $\sim$1.30.

6. Approximate Riemann solvers

In each of the methods presented here we make use of an approximate Riemann solver to obtain the local flux across a discontinuous interface. We will compare three approximate Riemann solvers, given in order of increasing complexity as Rusanov, Roe and AUSM$^+$-up.

It is a well-known (see, for example, [45]) result that the Roe solver is less dissipative than Rusanov's scheme. In general, dissipiation will be proportional to the wave speed of each characteristic flow variable, which is exaggerated in Rusanov's scheme by taking the wave speed of each wave to be equal to the largest wave speed. Roe's scheme, on the other hand, distinguishes all waves and hence provides a significantly tighter bound on the diffusivity. The AUSM$^+$-up scheme does not distinguish all waves, but instead uses asymptotic analysis and a separation of the advective and pressure terms in order to fight excess diffusivity at small Mach numbers. For details on specific Riemann solvers and their properties, we recommend Toro [42]. We only show the flux formulations in the x-direction. The numerical fluxes in the y-direction are analogous.

6.1. Rusanov

The Rusanov solution to the Riemann problem (first given in [34]) is perhaps the simplest to implement, using a straight flux difference between left and right edge values plus the maximum wave speed across the interface to regulate diffusion. Given left state vector $\mathbf{q}_L = (h_L,(hu)_L,(hv)_L)$ and right state vector $\mathbf{q}_R = (h_R,(hu)_R,(hv)_R)$, the Rusanov numerical flux in the x-direction assumes the form

$$\mathbf{F}^* = \frac{\mathbf{F}(\mathbf{q}_L) + \mathbf{F}(\mathbf{q}_R)}{2} - \frac{1}{2}\left|\lambda\left(\frac{\mathbf{q}_L + \mathbf{q}_R}{2}\right)\right|(\mathbf{q}_R - \mathbf{q}_L), \tag{56}$$

where, in the orthonormal frame,

$$\mathbf{F}(\mathbf{q}) = \begin{pmatrix} hu \\ hu^2 + \frac{1}{2}Gh^2 \\ huv \end{pmatrix} \tag{57}$$

is the flux function of the associated continuous equations (see (29)–(31)) and $|\lambda(\mathbf{q})|$ is the absolute value of the maximum wave speed. For the orthonormal shallow-water equations, one can quickly verify

$$|\lambda(\mathbf{q})| = |u| + \sqrt{Gh}. \tag{58}$$

As documented in the literature, the major downfall of the Rusanov scheme is its tendency for strong diffusivity compared with other approximate Riemann solvers. However, its ease of implementation and relative computational efficiency have resulted in its frequent use in numerical models.

6.2. Roe

The approximate Riemann solver of Roe [31] is ubiquitous in aerospace applications, but its use has been fairly limited in the atmospheric science community. A description of this method as applied to the shallow-water equations in Cartesian coordinates can be found in [2], for instance.

As with the Rusanov scheme, we are given left state vector $\mathbf{q}_L = (h_L,(hu)_L,(hv)_L)$ and right state vector $\mathbf{q}_R = (h_R,(hu)_R,(hv)_R)$ and must solve for the flux from the associated Riemann problem. We begin with the flux Jacobian in the x-direction for the orthonormal shallow-water equations, given by

$$\tilde{\mathbf{A}} = \frac{d\mathbf{F}}{d\mathbf{q}} = \begin{pmatrix} 0 & 1 & 0 \\ (Gh - u^2) & 2u & 0 \\ -uv & v & u \end{pmatrix}. \tag{59}$$

Following the approach of Roe, we construct a modified system of conservation laws with eigenvalues

$$\tilde{\lambda}^1 = \tilde{u} + \tilde{c}, \quad \tilde{\lambda}^2 = \tilde{u}, \quad \tilde{\lambda}^3 = \tilde{u} - \tilde{c}, \tag{60}$$

and corresponding eigenvectors

$$\mathbf{e}^1 = \begin{pmatrix} 1 \\ \tilde{u} + \tilde{c} \\ \tilde{v} \end{pmatrix}, \quad \mathbf{e}^2 = \begin{pmatrix} 0 \\ 0 \\ \tilde{c} \end{pmatrix}, \quad \mathbf{e}^3 = \begin{pmatrix} 1 \\ \tilde{u} - \tilde{c} \\ \tilde{v} \end{pmatrix}. \tag{61}$$

Here the eigenvalues and eigenvectors are written in terms of so-called Roe-averaged velocities $\tilde{u}$ and $\tilde{v}$ and the Roe-averaged gravity wave speed $\tilde{c}$, defined by

$$\tilde{u} = \frac{u_R + u_L w}{1 + w}, \quad \tilde{v} = \frac{v_R + v_L w}{1 + w}, \quad \tilde{c} = \sqrt{\frac{G(h_R + h_L)}{2}}, \tag{62}$$

where $w = \sqrt{h_L}/\sqrt{h_R}$.

The Roe numerical flux function then takes the form

$$\mathbf{F}^* = \frac{\mathbf{F}_R + \mathbf{F}_L}{2} - \frac{1}{2}\sum_{k=1}^{3} \tilde{\alpha}^k |\tilde{\lambda}^k| \tilde{e}^k, \tag{63}$$

where $\tilde{\alpha}^k$ are the coefficients obtained by decomposing the difference $\mathbf{q}_R - \mathbf{q}_L$ in terms of the basis of eigenvectors via

$$\mathbf{q}_R - \mathbf{q}_L = \sum_{k=1}^{3} \tilde{\alpha}^k \mathbf{e}^k. \tag{64}$$

They can be written in terms of the jumps $\Delta = (\,)_R - (\,)_L$ in the height and momentum field via

$$\tilde{\alpha}^1 = \frac{1}{2\tilde{c}}(\Delta(hu) - (\tilde{u} - \tilde{c})\Delta h), \tag{65}$$

$$\tilde{\alpha}^2 = \frac{1}{\tilde{c}}(\Delta(hv) - \tilde{v}\Delta h), \tag{66}$$

$$\tilde{\alpha}^3 = -\frac{1}{2\tilde{c}}(\Delta(hu) - (\tilde{u} + \tilde{c})\Delta h). \tag{67}$$

The Roe numerical flux tends to perform well for flows in the transsonic and supersonic regime but, similar to the Rusanov scheme, is generally diffusive for low-Mach number flows (see, for example, [15]).

6.3. AUSM$^+$-up

The AUSM$^+$-up approximate Riemann solver of [23] was recently developed with the purpose of improving numerical accuracy in the low-Mach number regime. In particular, the AUSM$^+$-up scheme works by splitting the advective component of the flux from the pressure component. We refer the reader to [23] for the mathematical details of this algorithm, instead giving a short overview of the implementation of this approach for the shallow-water equations.

Given left state vector $\mathbf{q}_L = (h_L,(hu)_L,(hv)_L)$ and right state vector $\mathbf{q}_R = (h_R,(hu)_R,(hv)_R)$, with orthonormal velocity components, we define the *averaged height*,

$$h_{1/2} = \frac{1}{2}(h_L + h_R), \tag{68}$$

averaged gravity wave speed,

$$a_{1/2} = \frac{1}{2}\left(\sqrt{gh_L} + \sqrt{gh_R}\right), \tag{69}$$

perpendicular Mach numbers at the interface,

$$M_L = \frac{u_L}{a_{1/2}} \quad \text{and} \quad M_R = \frac{u_R}{a_{1/2}}, \tag{70}$$

and *mean local Mach number*,

$$\overline{M}^2 = \frac{u_L^2 + u_R^2}{2a_{1/2}^2}. \tag{71}$$

The *advective component of the flux* is then defined by

$$\dot{m}_{1/2} = a_{1/2} M_{1/2} \begin{cases} h_L & \text{if } M_{1/2} > 0, \\ h_R & \text{otherwise}, \end{cases} \tag{72}$$

for some appropriate choice of the *interface Mach number* $M_{1/2}$. By defining

$$\mathcal{M}^{\pm}_{(2)}(M) = \frac{1}{4}(M \pm 1)^2, \quad \mathcal{M}^{\pm}_{(4)}(M) = \begin{cases} \frac{1}{2}(M \pm |M|) & \text{if } |M| \geqslant 1, \\ \mathcal{M}^{\pm}_{(2)}(M)(1 \mp 16\beta \mathcal{M}^{\mp}_{(2)}(M)) & \text{otherwise}, \end{cases} \tag{73}$$

we can obtain an expression for $M_{1/2}$ consistent with [23],

$$M_{1/2} = \mathcal{M}^{+}_{(4)}(M_L) + \mathcal{M}^{-}_{(4)}(M_R) - K_p \max(1 - \sigma\overline{M}^2, 0)\frac{G(h_R^2 - h_L^2)}{2h_{1/2}a_{1/2}^2}. \tag{74}$$

To obtain the *pressure-driven component of the flux*, we make use of the definition

$$\mathcal{P}^{\pm}_{(5)}(M) = \begin{cases} \frac{1}{2}(1 \pm \text{sign}(M)) & \text{if } |M| \geqslant 1, \\ \mathcal{M}^{\pm}_{(2)}(M)\left[(\pm 2 - M) \mp 16\alpha M \mathcal{M}^{\mp}_{(2)}(M)\right] & \text{otherwise}. \end{cases} \tag{75}$$

The interface pressure-driven flux is then given by

$$p_{1/2} = \mathcal{P}^{+}_{(5)}(M_L)p_L + \mathcal{P}^{-}_{(5)}(M_R)p_R - K_u \mathcal{P}^{+}_{(5)}(M_L)\mathcal{P}^{-}_{(5)}(M_R)(h_L + h_R)a_{1/2}(u_R - u_L). \tag{76}$$

Combining (72)–(74) and (76), we obtain that the total numerical flux across the interface in the x-direction is then given by

$$\mathbf{F}^* = \left[\dot{m}_{1/2} \begin{cases} \mathbf{\Psi}_L & \text{if } \dot{m}_{1/2} > 0, \\ \mathbf{\Psi}_R & \text{otherwise} \end{cases}\right] + \mathbf{p}_{1/2}, \tag{77}$$

with

Table 2
Relative errors in the height field h for [46] test case 1 – advection of a cosine bell (at a resolution of $40 \times 40 \times 6$ and after $t = 12$ days) for the FV3s scheme (top) and FV4 scheme (bottom).

CFL	Direction	L_1 error	L_2 error	L_∞ error	Maximum	Minimum
FV3s method						
1.0	$\alpha = 0°$	1.03060(−1)	6.68703(−2)	4.94155(−2)	−3.49156(−2)	−2.76913(−2)
	$\alpha = 45°$	1.02219(−1)	6.42548(−2)	5.01053(−2)	−3.14562(−2)	−2.42758(−2)
0.5	$\alpha = 0°$	4.87889(−2)	2.95893(−2)	2.34241(−2)	−6.66680(−3)	−1.59017(−2)
	$\alpha = 45°$	4.49184(−2)	2.55575(−2)	1.89556(−2)	−5.48348(−3)	−1.00990(−2)
FV4 method						
1.0	$\alpha = 0°$	4.42623(−2)	2.69819(−2)	2.30115(−2)	1.50290(−4)	−2.25188(−2)
	$\alpha = 45°$	4.21728(−2)	2.36737(−2)	1.86956(−2)	1.51660(−3)	−1.48344(−2)
0.5	$\alpha = 0°$	3.83263(−2)	2.31939(−2)	1.99693(−2)	−8.35479(−5)	−1.92501(−2)
	$\alpha = 45°$	3.50956(−2)	1.96006(−2)	1.41711(−2)	3.51985(−4)	−1.25210(−2)

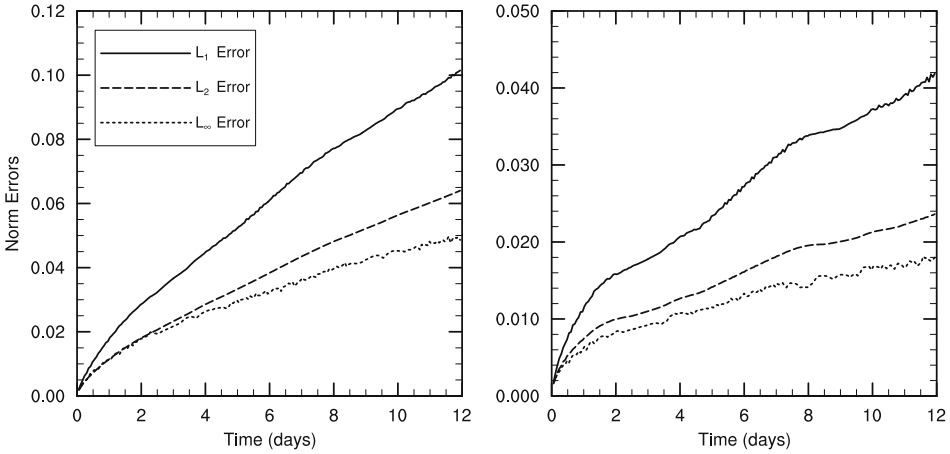

Fig. 5. Time series of the normalized errors for the cosine bell advection test case with FV3s method (left) and FV4 method (right) in the direction $\alpha = 45°$ for one rotation (12 days) with CFL = 1.0 on a $40 \times 40 \times 6$ grid. Note the difference in the vertical scales of these plots.

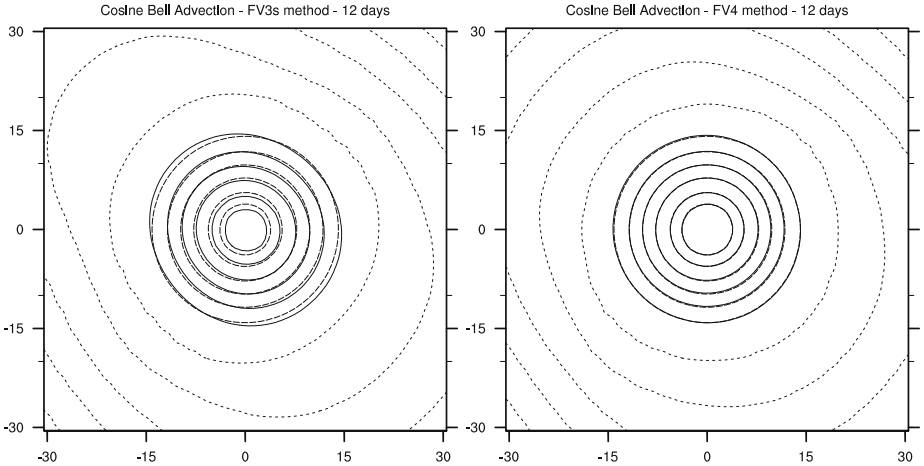

Fig. 6. Reference height field (long-dashed line) and numerically computed height field (solid line) with FV3s method (left) and FV4 method (right) in the direction $\alpha = 45°$ after one rotation (12 days). Contours are from 0 m to 800 m in intervals of 160 m with the zero contour of the numerically computed solution shown as a dotted line so as to emphasize the numerical oscillations. The direction of motion is to the bottom-right.

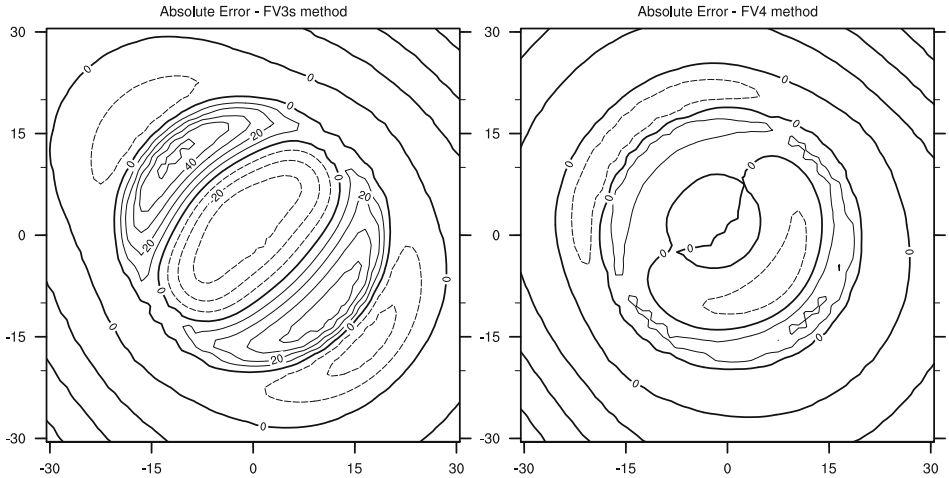

Fig. 7. Difference between the numerically computed solution and true solution with FV3s method (left) and FV4 method (right) in the direction $\alpha = 45°$ after one rotation (12 days) and at a resolution of $40 \times 40 \times 6$. Contours are in intervals of 10 m with solid lines denoting positive contours and dashed lines denoting negative contours. The zero line is enhanced.

$$\Psi_L = \begin{pmatrix} 1 \\ u_L \\ v_L \end{pmatrix}, \quad \Psi_R = \begin{pmatrix} 1 \\ u_R \\ v_R \end{pmatrix}, \quad \mathbf{p}_{1/2} = \begin{pmatrix} 0 \\ p_{1/2} \\ 0 \end{pmatrix}. \tag{78}$$

Several free parameters are available in this scheme. For simplicity, we follow [23] by choosing

$$\alpha = \frac{3}{16}, \quad \beta = \frac{1}{8}, \quad K_p = \frac{1}{4}, \quad \sigma = 1. \tag{79}$$

The constant K_u, which governs velocity diffusivity, does not seem to play a major role in these results and is chosen to be zero.

The AUSM$^+$-up flux has been constructed with the goal of improving convergence and accuracy in the low-Mach number limit ($M \to 0$), and so we anticipate it to be less diffusive than Rusanov or Roe in this regime.

7. Numerical results

For all calculations we use a normalized length scale in terms of Earth radii and use time given in days. For the Earth the physical parameters under these scalings are given by

Table 3
Relative errors in the height field h for [46] test case 2 – Geostrophically balanced flow (at $t = 5$ days with $\alpha = 45°$) for the FV3s scheme with Rusanov, Roe and AUSM$^+$-up Riemann solvers. The computed order of accuracy is obtained from a least squares fit through the data.

Resolution (N_c)	L_1 error	L_2 error	L_∞ error
Rusanov solver			
20	1.86793(−4)	2.65483(−4)	8.52171(−4)
40	2.42357(−5)	3.42298(−5)	1.06972(−4)
80	3.05468(−6)	4.31159(−6)	1.36274(−5)
160	3.82801(−7)	5.40185(−7)	1.83789(−6)
Order	2.978	2.981	2.954
Roe solver			
20	1.97019(−4)	2.78152(−4)	8.28123(−4)
40	2.56497(−5)	3.65241(−5)	1.20533(−4)
80	3.23454(−6)	4.61740(−6)	1.82294(−5)
160	4.05309(−7)	5.79033(−7)	2.49317(−6)
Order	2.976	2.971	2.785
AUSM$^+$-up solver			
20	1.29301(−4)	1.84921(−4)	5.84845(−4)
40	1.68287(−5)	2.41594(−5)	8.20936(−5)
80	2.12139(−6)	3.05250(−6)	1.22420(−5)
160	2.65731(−7)	3.82725(−7)	1.67872(−6)
Order	2.977	2.973	2.808

Table 4
As Table 3 except with the FV4 scheme.

Resolution (N_c)	L_1 error	L_2 error	L_∞ error
Rusanov solver			
20	1.23147(−5)	1.83684(−5)	5.28083(−5)
40	3.92605(−7)	6.14237(−7)	3.30766(−6)
80	1.42768(−8)	2.19348(−8)	1.94550(−7)
160	6.44784(−10)	9.23157(−10)	1.09139(−8)
Order	4.744	4.765	4.081
Roe solver			
20	3.33670(−6)	4.71855(−6)	1.33113(−5)
40	1.56059(−7)	2.14543(−7)	5.63099(−7)
80	8.67290(−9)	1.17659(−8)	2.79641(−8)
160	5.19851(−10)	7.03778(−10)	1.62477(−9)
Order	4.211	4.232	4.333
AUSM$^+$-up solver			
20	3.26183(−6)	4.66310(−6)	1.19600(−5)
40	1.54530(−7)	2.14661(−7)	5.14470(−7)
80	8.65658(−9)	1.18352(−8)	2.70597(−8)
160	5.19867(−10)	7.06975(−10)	1.64234(−9)
Order	4.200	4.224	4.274

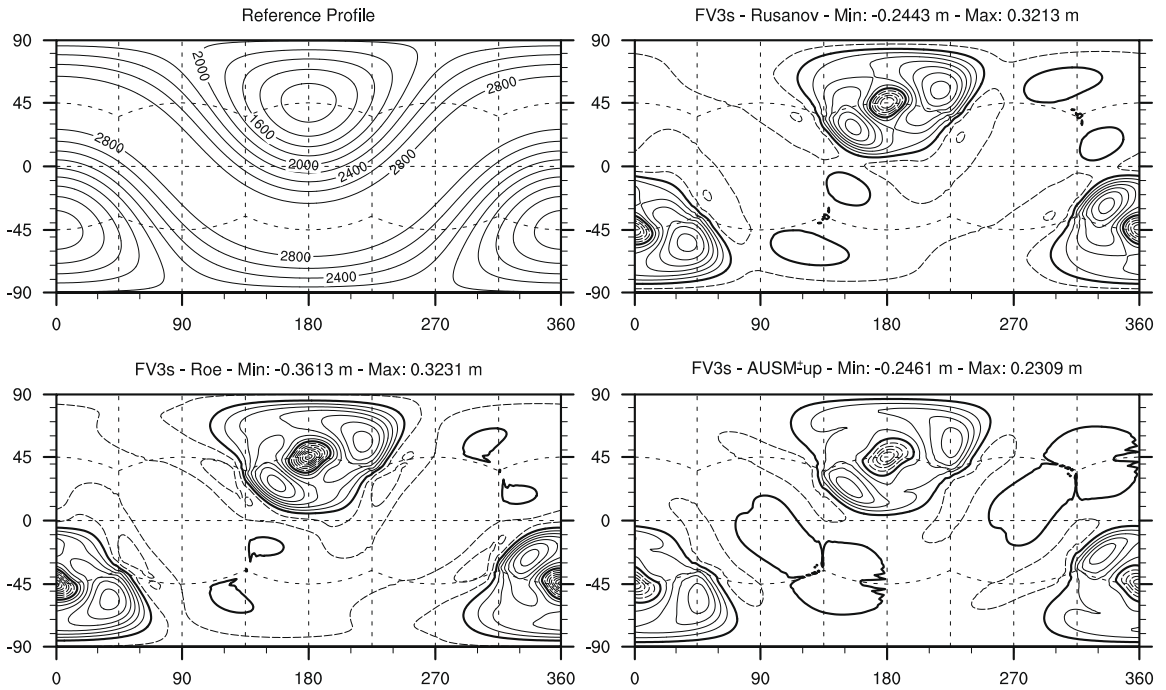

Fig. 8. Background height field (top-left, in m) and absolute errors associated with the FV3s scheme on a $40 \times 40 \times 6$ grid with Rusanov (top-right), Roe (bottom-left) and AUSM$^+$-up (bottom-right) solvers for [46] test case 2 with $\alpha = 45°$. Contour lines are in units of 5×10^{-2} m, with solid lines corresponding to positive values and long-dashed lines corresponding to negative values. The thick line corresponds to zero error. The short dashed lines show the location of the underlying cubed-sphere grid.

$$G = 11489.57 \text{ Earth radii/day}^2 \quad \text{and} \quad \Omega = 6.300288 \text{ day}^{-1}. \tag{80}$$

Unless stated otherwise we make use of a CFL number of 1.0 for all simulations.

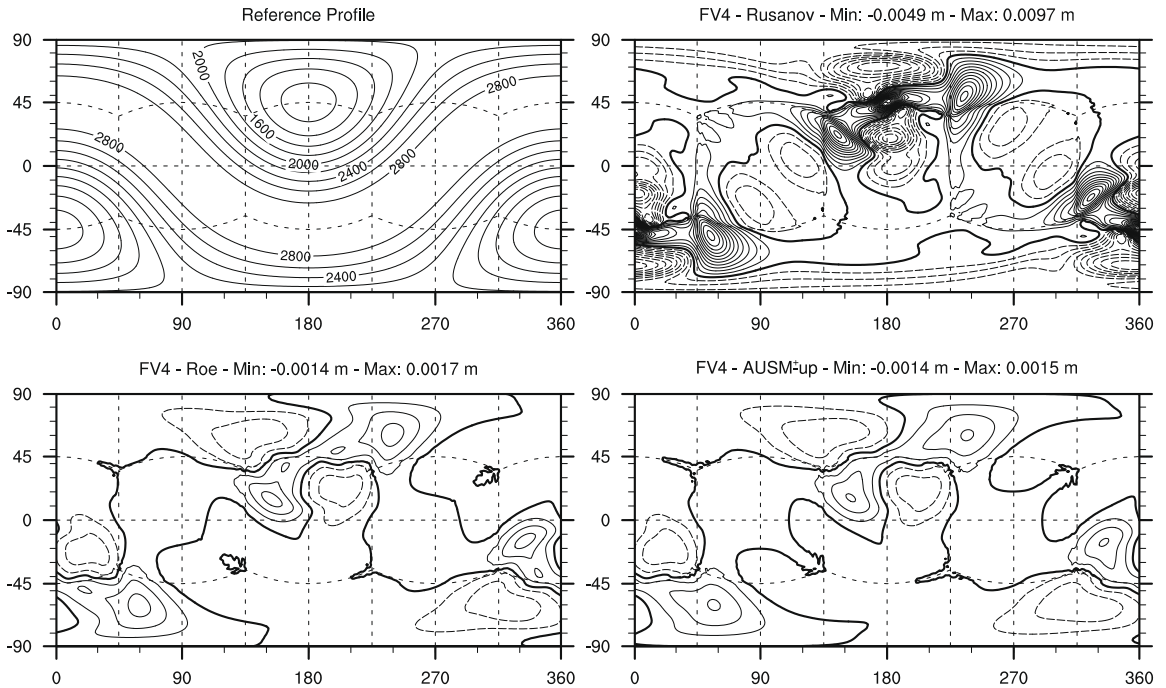

Fig. 9. As Fig. 8 except using the FV4 scheme. Contour lines are in units of 5×10^{-4} m.

Error measures are calculated in the height field via the usual global error norms,

$$\ell_1(h) = \frac{I[|h - h_T|]}{I[|h_T|]}, \tag{81}$$

$$\ell_2(h) = \sqrt{\frac{I\left[(h - h_T)^2\right]}{I[h_T^2]}}, \tag{82}$$

$$\ell_\infty(h) = \frac{\max|h - h_T|}{\max|h_T|}, \tag{83}$$

where h_T is the reference (true) height field and I denotes an approximation to the global integral, given by

$$I[x] = \sum_{\text{all cells}\ k} x_k A_k, \tag{84}$$

with A_k denoting the area of element k. For the advection test case we also make use of the relative maximum and minimum,

$$\langle \text{Relative Maximum} \rangle = \frac{\max h - \max h_T}{\max|h_T|}, \tag{85}$$

$$\langle \text{Relative Minimum} \rangle = \frac{\min h - \min h_T}{\max|h_T|}. \tag{86}$$

Table 5
Relative errors in the height field h for [46] test case 3 – Geostrophically balanced flow with compact support (at $t = 5$ days with $\alpha = 60°$) for the FV3s scheme with Rusanov, Roe and AUSM$^+$-up Riemann solvers. The computed order of accuracy is obtained from a least squares fit through the data.

Resolution (N_c)	L_1 error	L_2 error	L_∞ error
Rusanov solver			
20	5.29489(−4)	1.04318(−3)	6.98472(−3)
40	4.14616(−5)	7.62192(−5)	4.36449(−4)
80	4.90936(−6)	8.83443(−6)	4.42438(−5)
160	6.24068(−7)	1.11900(−6)	5.91343(−6)
Order	3.226	3.270	3.392
Roe solver			
20	1.72217(−4)	3.13719(−4)	1.60254(−3)
40	1.79322(−5)	3.39544(−5)	1.93667(−4)
80	2.41481(−6)	4.62184(−6)	2.70813(−5)
160	3.09483(−7)	5.94444(−7)	3.46030(−6)
Order	3.025	3.001	2.940
AUSM$^+$-up solver			
20	1.47699(−4)	2.71802(−4)	1.26574(−3)
40	1.89854(−5)	3.69259(−5)	2.24091(−4)
80	2.61576(−6)	5.16111(−6)	3.13437(−5)
160	3.36013(−7)	6.64243(−7)	4.00544(−6)
Order	2.920	2.887	2.775

Table 6
As Table 5 except with the FV4 scheme.

Resolution (N_c)	L_1 error	L_2 error	L_∞ error
Rusanov solver			
20	3.95805(−4)	7.38801(−4)	4.44070(−3)
40	1.65282(−5)	3.13826(−5)	1.89074(−4)
80	5.41290(−7)	1.02393(−6)	5.96072(−6)
160	1.70040(−8)	3.19845(−8)	1.79530(−7)
Order	4.845	4.842	4.877
Roe solver			
20	1.22144(−4)	2.35850(−4)	1.28707(−3)
40	4.48290(−6)	8.67097(−6)	4.67861(−5)
80	1.50958(−7)	2.89663(−7)	1.50027(−6)
160	5.49471(−9)	1.04223(−8)	5.04890(−8)
Order	4.821	4.830	4.888
AUSM$^+$-up solver			
20	1.01946(−4)	2.01244(−4)	1.22075(−3)
40	3.76651(−6)	7.45425(−6)	4.44324(−5)
80	1.29063(−7)	2.53563(−7)	1.44834(−6)
160	4.93269(−9)	9.55944(−9)	4.99077(−8)
Order	4.787	4.796	4.867

7.1. Advection of a cosine bell

The first test case of [46] simulates the advection of a cosine bell through one rotation around the sphere over a 12-day time period. The prescribed wind field is nondivergent, and so the flux-form continuity equation in orthonormal form,

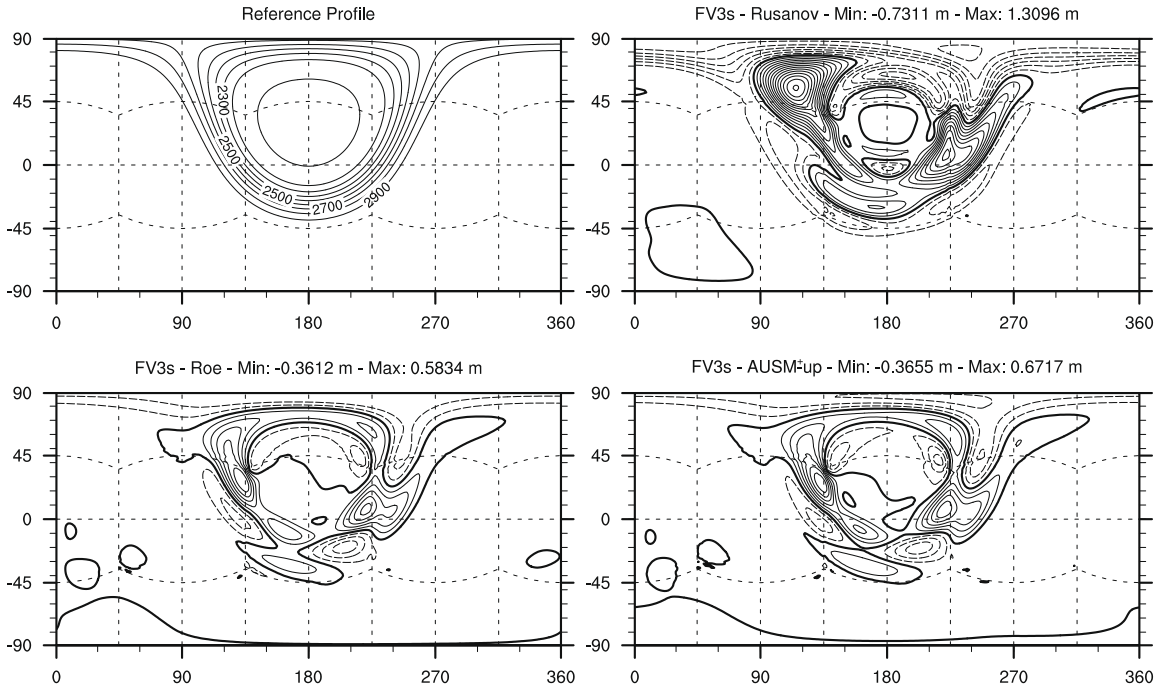

Fig. 10. Background height field (top-left, in m) and absolute errors associated with the FV3s scheme on a $40 \times 40 \times 6$ grid with Rusanov (top-right), Roe (bottom-left) and AUSM$^+$-up (bottom-right) Riemann solvers for [46] test case 3 with $\alpha = 60°$. Contour lines are in units of 10^{-1} m, with solid lines corresponding to positive values and dashed lines corresponding to negative values. The thick line corresponds to zero error.

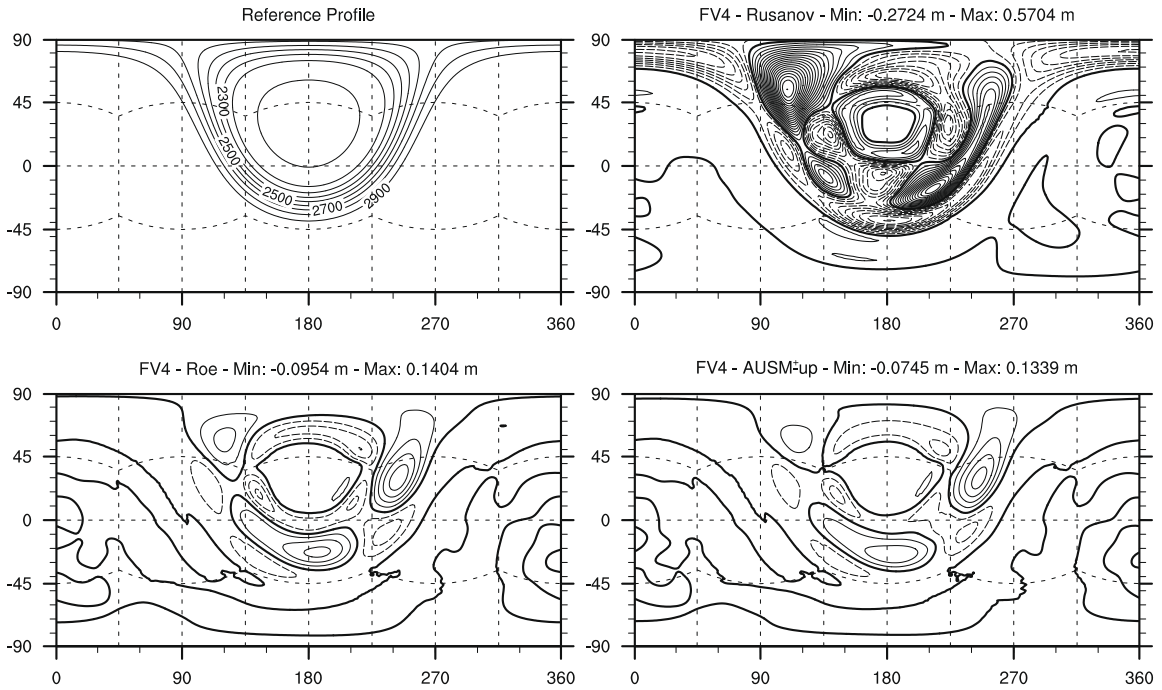

Fig. 11. As Fig. 10 except using the FV4 scheme. Contour lines are in units of 3×10^{-2} m.

$$\frac{\partial h}{\partial t} + \frac{\partial}{\partial x}(hu) + \frac{\partial}{\partial y}(hv) = 0, \tag{87}$$

represents an advection equation for the tracer distribution. Here, x and y denote the components of the coordinate vector within the orthonormal frame. The velocity vector is not evolved, and is instead obtained by directly evaluating the velocity field as needed. For this equation the Riemann flux solution reduces to

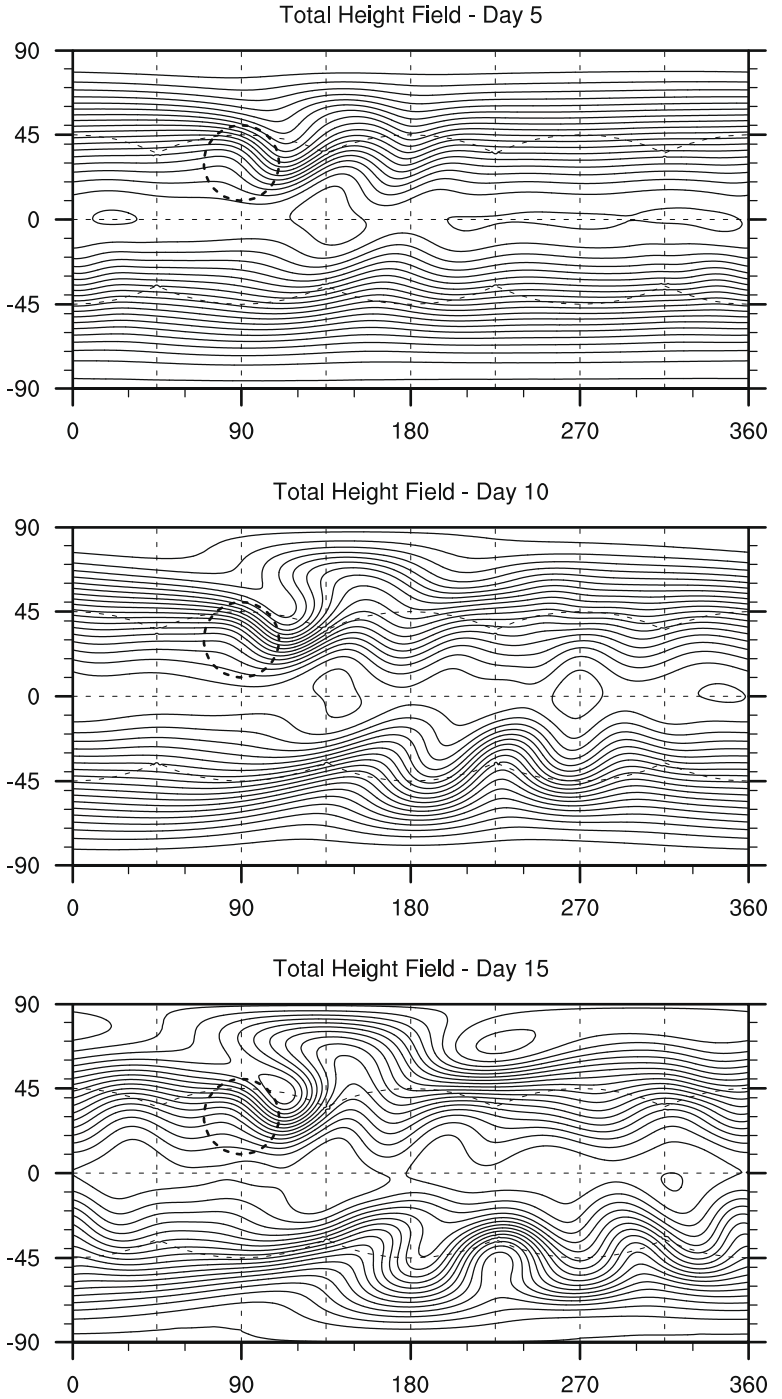

Fig. 12. Total height field for [46] test case 5. We show the simulation results for the FV4 scheme with AUSM$^+$-up Riemann solver simulated on a $40 \times 40 \times 6$ grid. The dashed circle represents the location of the conical mountain. Contour levels are from 5050 m to 5950 m in intervals of 50 m, with the highest elevation being near the equator (the small enclosed contours). The results for the FV3s scheme are visually identical.

$$F^* = \begin{cases} h_L u & \text{if } u > 0, \\ h_R u & \text{if } u < 0. \end{cases} \tag{88}$$

The initial height field is given by

$$h = \begin{cases} \left(\frac{h_0}{2}\right)\left(1 + \cos\frac{\pi r}{R}\right) & \text{if } r < R, \\ 0 & \text{otherwise}, \end{cases} \tag{89}$$

where r is the great circle distance from the center of the height profile. The free parameters are given as $h_0 = 1000$ m $= 1.5696 \times 10^{-4}$ Earth radii and $R = \frac{1}{3}$ Earth radii. The divergence-free velocity field is given in terms of spherical coordinates as

$$u_\lambda = u_0(\cos\theta\cos\alpha + \cos\lambda\sin\theta\sin\alpha), \tag{90}$$

$$u_\theta = -u_0\sin\lambda\sin\alpha, \tag{91}$$

where $u_0 = (\pi/6)$ Earth radii/day. Here the parameter α denotes the rotation angle transcribed between the physical north pole and the center of the northern panel on the cubed-sphere grid (and should not be confused with the equiangular coordinate α).

This test case is particularly useful at verifying accuracy of the panel boundaries. We give the relative errors after one rotation in Table 2 using $\Delta t = 90$ min (CFL = 1.0) and $\Delta t = 45$ min (CFL = 0.5), and the corresponding time series of these errors (with CFL = 1.0) in Fig. 5. In all cases we use a resolution of $40 \times 40 \times 6$. A graphical comparison of the reference field and results after one rotation at $\alpha = 45^\circ$ are given in Fig. 6 and absolute differences in Fig. 7. These results do not show any obvious noise due to the patch boundaries and the numerical errors we observe are essentially independent of the flow direction. As expected, identical error measures at $\alpha = 0$ and $\alpha = \pi/2$ are observed and so are not repeated. Interestingly, we do observe a significant sensitivity of the method due to choice of the CFL number (see Table 2) with halving of the CFL number leading to a decrease of more than half in the error norms for the FV3s scheme.

No attempt to include a monotonicity filter was made in these results, which leads to obvious overshoots and undershoots of the cosine bell profile and oscillations in the tracer field away from the cosine bell profile. These errors

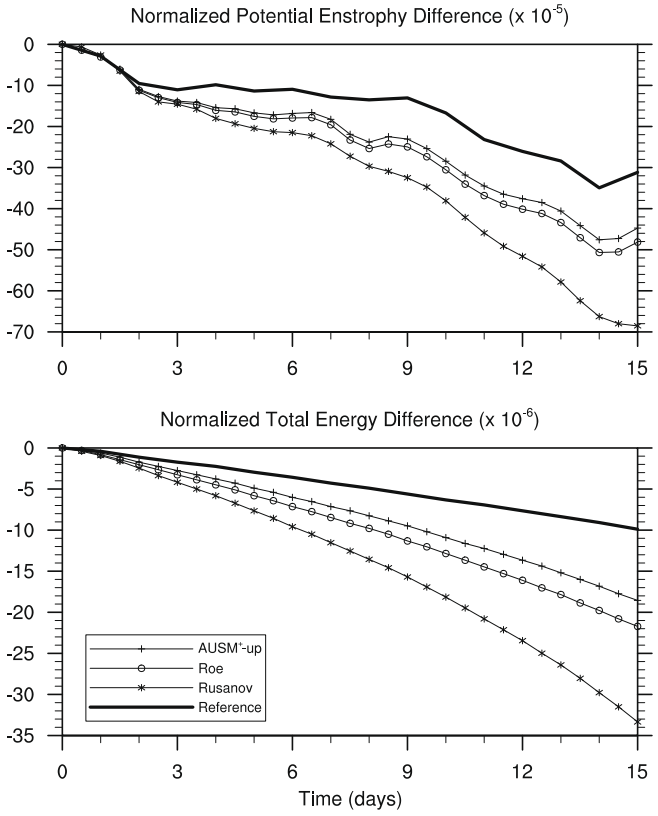

Fig. 13. Normalized potential enstrophy (top) and total energy (bottom) difference for the flow over an isolated mountain test case using the FV3s scheme simulated on a $40 \times 40 \times 6$ grid.

are reduced in the FV4 scheme. The error norms presented here are competitive with existing numerical methods of equivalent order-of-accuracy.

7.2. Steady-state geostrophically balanced flow

Test case 2 of [46] simulates a zonally symmetric geostrophically balanced flow. The analytic height field, in terms of latitude θ and longitude λ, is given by

$$h = h_0 - \frac{1}{G}\left(\Omega u_0 + \frac{u_0^2}{2}\right)(-\cos\lambda\cos\theta\sin\alpha + \sin\theta\cos\alpha)^2, \tag{92}$$

with background height h_0 and background velocity u_0 chosen to be

$$h_0 = 4.7057 \times 10^{-4} \text{ Earth radii} \quad \text{and} \quad u_0 = \frac{\pi}{6} \text{ Earth radii/day}. \tag{93}$$

As in Section 7.1, the parameter α denotes the angle transcribed between the physical north pole and the center of the northern panel. The background velocity field is the same as in (90) and (91). This test case represents an unstable equilibrium solution to the shallow-water equations, and so is not preserved in the long-term in most atmospheric models. However, it is useful to use this test case to study the convergence properties of a given numerical method.

We use high-order Gaussian quadrature to initialize the height and momentum fields in the numerical model and run the model for 5 days. The timestep at $40 \times 40 \times 6$ resolution for this case is $\Delta t = 16.5$ min. The results of the convergence study for the three schemes with all approximate Riemann solvers is given in Tables 3 and 4 using $\alpha = 45°$. We see third-order convergence for the dimension-split FV3s scheme and super-convergence above order 4 for the FV4 scheme. When looking at the approximate Riemann solvers, we see significantly different results for the FV3s scheme and the FV4 scheme. For the FV3s scheme the error norms do not differ substantially, and we actually observe the Roe solver performing slightly worse than the Rusanov solver. The FV4 scheme instead shows a significant improvement in error norms when using the Roe or AUSM$^+$-up flux over the Rusanov flux. The high-order-of-accuracy for the Rusanov flux is attributed to the improvement in continuity of the reconstruction, so we do not expect the error norms from the Rusanov solver to be less than those of the Roe or AUSM$^+$-up flux. The actual error norms presented here are competitive with existing methods (see [8,33,41]).

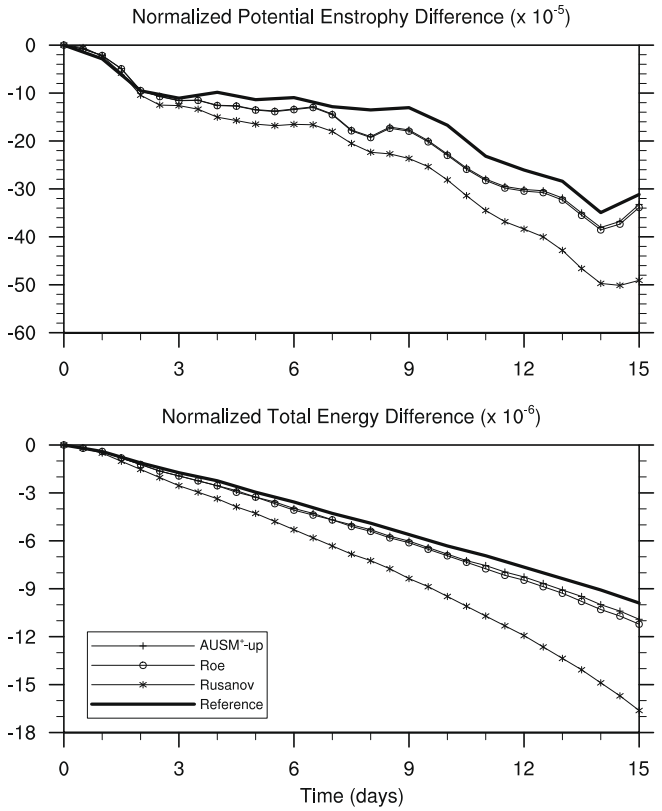

Fig. 14. Normalized potential enstrophy (top) and total energy (bottom) difference for the flow over an isolated mountain test case using the FV4 scheme simulated on a $40 \times 40 \times 6$ grid.

Error plots are given in Figs. 8 and 9. The clear diffusivity of the Rusanov solver is apparent here, especially in the FV4 scheme where Rusanov demonstrates approximately five times worse errors than the other fluxes. In this case errors at the panel corners appear to be greatly enhanced. We see very little difference between the error distribution for the Roe and AUSM$^+$-up solvers.

7.3. Steady-state geostrophically balanced flow with compact support

Test case 3 of [46] again simulates a geostrophically balanced flow, but this time with a height field that has compact support. The analytic velocity field is given in rotated latitude–longitude coordinates (θ', λ') (with rotation angle α) by

$$u'_\lambda = u_0 b(x) b(x_e - x) \exp(4/x_e) \quad \text{and} \quad u'_\theta = 0, \tag{94}$$

where

$$b(x) = \begin{cases} 0 & \text{if } x \leqslant 0, \\ \exp(-1/x) & \text{if } 0 < x. \end{cases} \tag{95}$$

and

$$x = x_e \frac{(\theta' - \theta_b)}{(\theta_e - \theta_b)}. \tag{96}$$

The details of the rotated coordinate system are described in [46]. The analytic height field is given by

$$h = h_0 - \frac{1}{G} \int_{-\pi/2}^{\theta'} \left(2\Omega \sin\tau + u'_\lambda(\tau) \tan\tau\right) u'_\lambda(\tau) d\tau, \tag{97}$$

which must be integrated numerically at each point where h is desired. The background height and velocity fields are again chosen to be

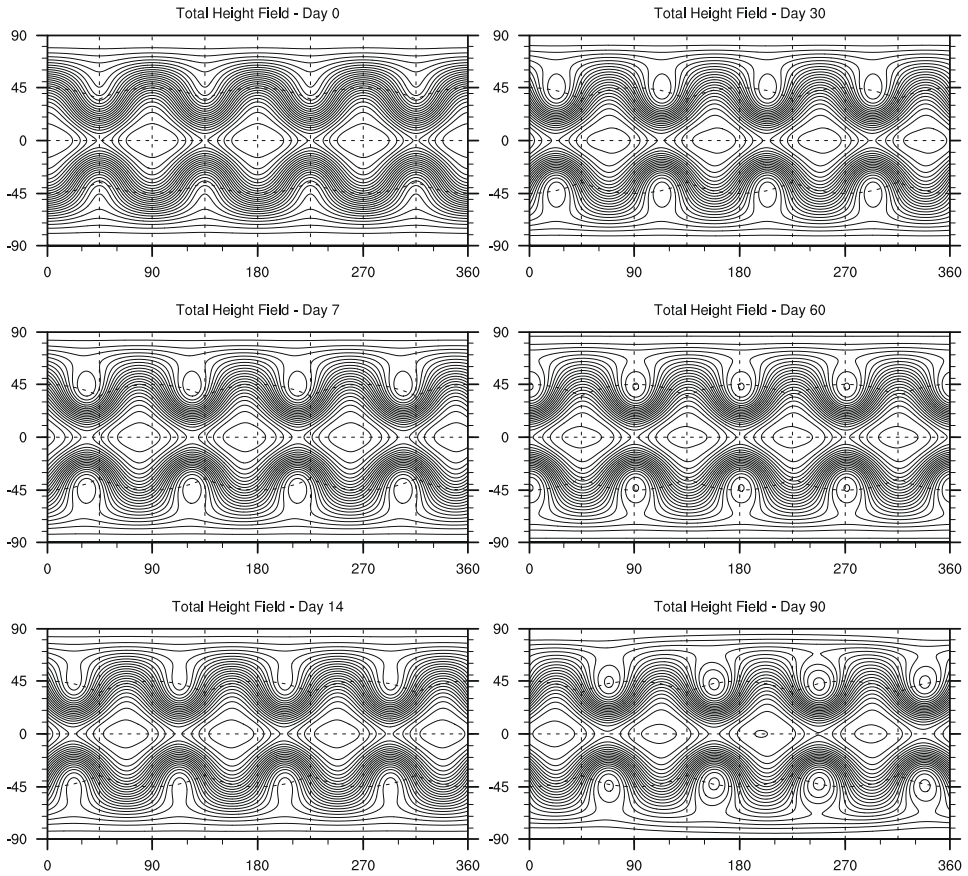

Fig. 15. Wavenumber four Rossby–Haurwitz wave (test case 6 in [46]). The solution is computed on a $80 \times 80 \times 6$ grid using the FV3s scheme with AUSM$^+$-up solver on day 0, 7 and 14 (left column, from top to bottom) and day 30, 60 and 90 (right column, from top to bottom). The contour interval is 100 m, with the innermost contours being the highest (10, 500 m). The lowermost contours at day 0, 7, 14 are 8100 m, 8300 m and 8200 m, respectively.

$$h_0 = 4.7057 \times 10^{-4} \text{ Earth radii} \quad \text{and} \quad u_0 = \frac{\pi}{6} \text{ Earth radii/day}. \tag{98}$$

Further, the compact height field is determined by the parameters

$$\theta_b = -\frac{\pi}{6}, \quad \theta_e = \frac{\pi}{2}, \quad \text{and} \quad x_e = 0.3. \tag{99}$$

This test case again represents an unstable equilibrium solution to the shallow-water equations, and so is not preserved in the long-term in most atmospheric models. We again use high-order Gaussian quadrature to initialize the height and momentum fields in the numerical model and run the model for 5 days. In all cases we make use of a rotation angle of 60°. The timestep at $40 \times 40 \times 6$ resolution for this case is $\Delta t = 17.5$ min.

The results of the convergence study for the two schemes with all Riemann solvers is given in Tables 5 and 6. Again we see similar convergence rates to that of test case 2, except noting that we see a significant gain in accuracy (a $3\times$ improvement in the L_1 norm) when going from the Rusanov Riemann solver to either the Roe or AUSM$^+$-up Riemann solver. For the FV3s scheme we observe slightly better performance from the Roe solver over AUSM$^+$-up, and the opposite for the FV4 scheme.

Error plots are given in Figs. 10 and 11. The error plots from the Roe and AUSM$^+$-up Riemann solvers are very similar, as expected given their similar error norms. However, we see very strong error due to diffusivity in the results from the Rusanov scheme of almost an order of magnitude more than the other two approaches.

7.4. Zonal flow over an isolated mountain

Test case 5 in [46] considers flow with a topographically driven source term. The wind and height fields are defined as in Section 7.2, except with $\alpha = 0$, $h_0 = 5960$ m and $u_0 = 20$ m/s. A conical mountain is introduced into the flow, given by

$$z = z_0(1 - r/R), \tag{100}$$

with $z_0 = 2000$ m, $R = \pi/9$ and $r^2 = \min[R^2, (\lambda - \lambda_c)^2 + (\theta - \theta_c)^2]$. The center of the mountain is taken as $\lambda_c = 3\pi/2$ and $\theta_c = \pi/6$.

We plot the height field at day 5, 10 and 15 in Fig. 12 on a $40 \times 40 \times 6$ grid with a timestep of 12.5 min.

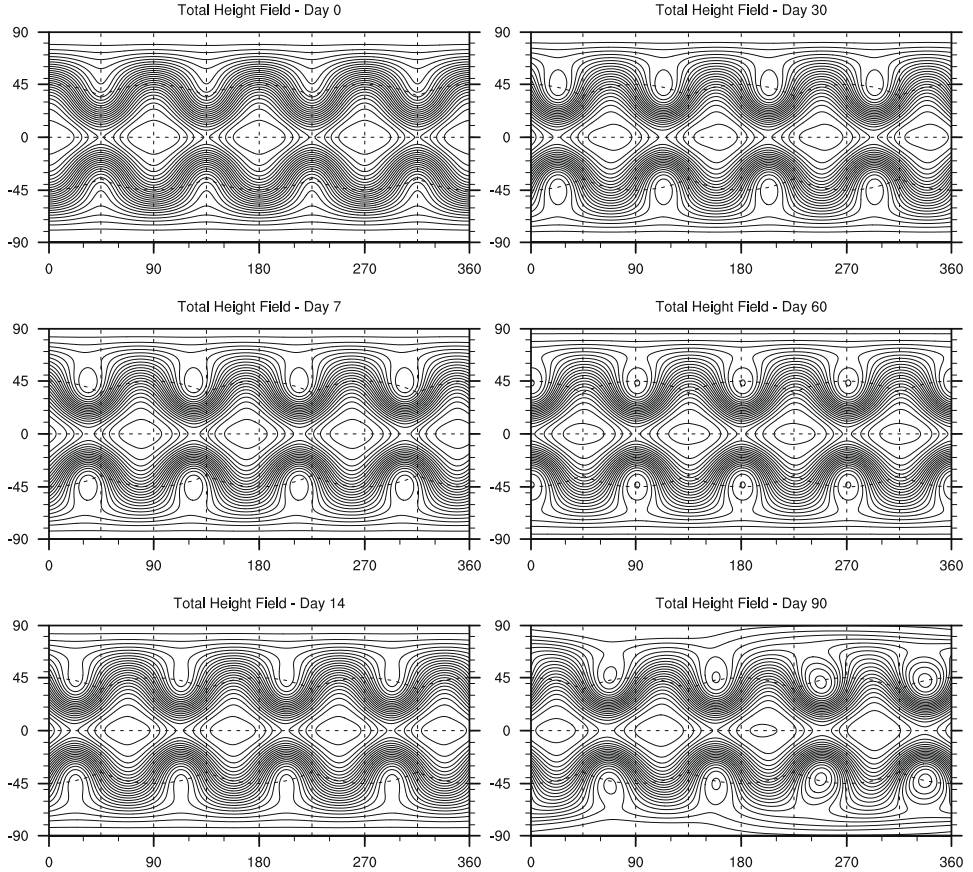

Fig. 16. As Fig. 15 except for the FV4 scheme.

Potential enstrophy ξ and total energy E are invariant under the shallow-water equations, and are defined by

$$\xi = \frac{(\zeta + f)^2}{2h} \quad \text{and} \quad E = \frac{1}{2} h \mathbf{v} \cdot \mathbf{v} + \frac{1}{2} G(H^2 - z^2). \tag{101}$$

From the element-averages of the height and momentum field, we calculate total energy directly, weighting element-wise totals by element area. Similarly, potential enstrophy is calculated by using a central-difference approximation to the curl and then using element-averages. The resulting computed invariants are accurate up to $O(\Delta^2)$.

We compare our results with the reference solution of [17], which is run on the spectral transform shallow-water model (STSWM) at T426 resolution. This high resolution reference solution was computed by the German Weather Service (DWD) and is available online (http://icon.enes.org/swm/stswm/node5.html). The T426 simulation utilized a Gaussian grid with 640×1280 grid points in latitudinal and longitudinal direction which corresponds to a grid spacing of about 31 km at the equator. To directly compare with our model, the spectral coefficients from STSWM are sampled on the cubed-sphere grid at high-resolution Gaussian quadrature points in order to obtain element-averages of the state variables on a $40 \times 40 \times 6$ grid. Invariants are then calculated from the resampled cubed-sphere solution and our own cubed-sphere runs using standard difference operators.

The normalized total potential enstrophy and total energy difference from the initial state versus time are given for the FV3s scheme in Fig. 13 and for the FV4 scheme in Fig. 14. We observe very good performance of both schemes with respect to conservation of these quantities, with the best conservation properties coming from the AUSM$^+$-up Riemann solver (the Roe Riemann solver also matches very closely). The Rusanov Riemann solver performs significantly worse in all cases, due to the significant diffusion in this scheme.

7.5. Rossby–Haurwitz wave

The Rossby–Haurwitz wave (test case 6 in [46]) is an analytic solution of the nonlinear barotropic vorticity equation on the sphere. The height and velocity field can be analytically computed with several free parameters, however for the purposes of testing the numerical model we only make use of the wave number 4 test. Our parameters are analogous to those of [46], who also provides expressions for the analytic fields for this test case. Again, we make use of high-order Gaussian quadrature to calculate the initial height and momentum fields.

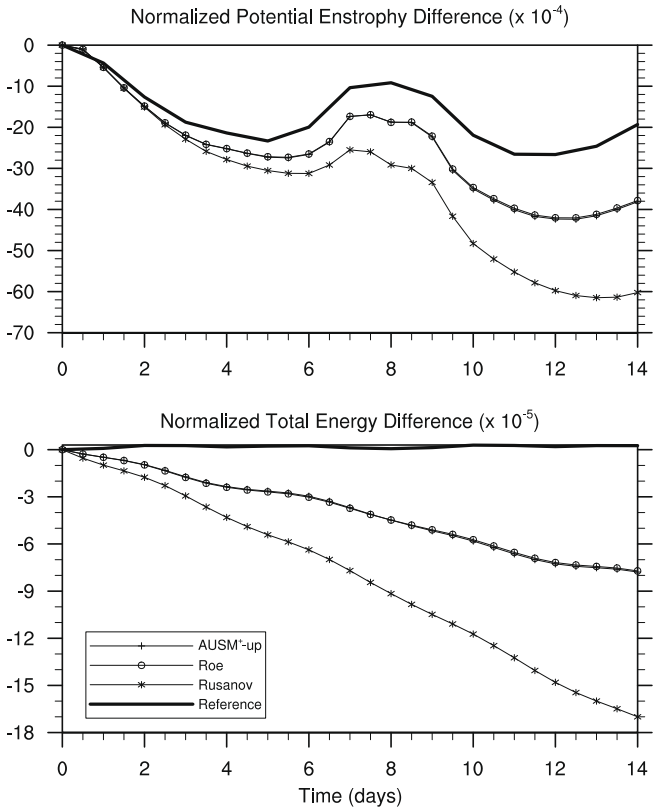

Fig. 17. Normalized potential enstrophy (top) and potential energy (bottom) difference for the Rossby–Haurwitz wave test case using the FV3s method simulated on a $40 \times 40 \times 6$ grid.

It is well known that the wave number 4 Rossby–Haurwitz wave is susceptible to instability which can be driven by truncation error in the initial conditions (see, for example, [40]), and hence will eventually collapse into a turbulent flow. The time of the breakdown varies based on the numerical scheme employed and the choice of grid resolution. For the FV3s and FV4 schemes discussed in this paper, we begin to see breakdown at about day 80, but find that adding perturbations on the order of the scheme's truncation error can drive the collapse to as early as day 30.

We plot the height field for the FV3s scheme in Fig. 15 and for the FV4 scheme in Fig. 16 at day 0, 7, 14, 30, 60 and 90 at a resolution of $80 \times 80 \times 6$. The higher resolution is required for the plots to capture some of the small scale features of the wave profile. The total energy and potential enstrophy computed at each day of the simulation (up to day 14) is presented in Figs. 17 and 18, compared against the STSWM reference solution at T511 (26 km) resolution truncated to the cubed-sphere at $40 \times 40 \times 6$ for consistency with Figs. 13 and 14. The timestep is chosen to be 4.2 min for the $80 \times 80 \times 6$ runs and 8.4 min for the $40 \times 40 \times 6$ runs. Again, the Roe and AUSM$^+$-up Riemann solvers perform very well, whereas the Rusanov Riemann solver performs noticably worse. The finite-volume nature of the underlying scheme imposes fairly strong diffusivity on the energy when compared to the reference solution, but nonetheless we observe similar conservation properties to competing schemes.

7.6. Barotropic instability

The barotropic instability test case of [12] consists of a zonal jet with compact support at a latitude of 45°. A small height disturbance is added which causes the jet to become unstable and collapse into a highly vortical structure. The relative vorticity is used here as a comparison between the solution presented in [12] (obtained via a spectral transform method) and the solution obtained by direct simulation. We present the potential vorticity at varying resolutions for the FV3s and FV4 scheme with AUSM$^+$-up Riemann solver in Figs. 19 and 20, respectively. The timestep used for this test case is 9 min at a resolution of $40 \times 40 \times 6$. No artificial viscosity is added in our simulation, since the numerical diffusion introduced by the finite-volume method is sufficient to ensure stability.

As observed by St-Cyr et al. [36], this test case is particularly difficult for models using the cubed-sphere to handle. Since the jet passes over cubed-sphere panel edges eight times and is driven by a relatively mild perturbation, wave number four grid forcing is significant in disturbing the collapse for resolutions less than approximately $100 \times 100 \times 6$. For higher

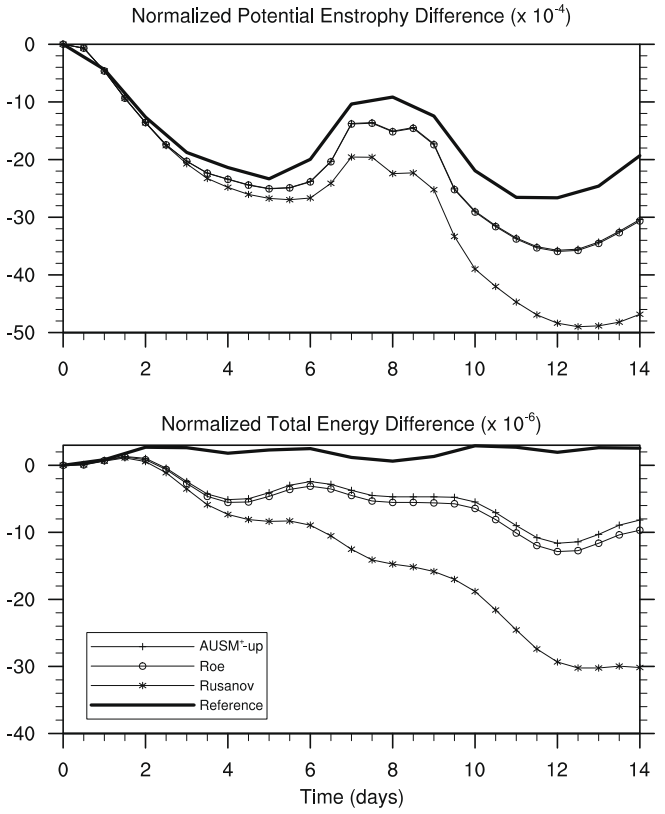

Fig. 18. Normalized potential enstrophy (top) and potential energy (bottom) difference for the Rossby–Haurwitz wave test case using the FV4 simulated on a $40 \times 40 \times 6$ grid.

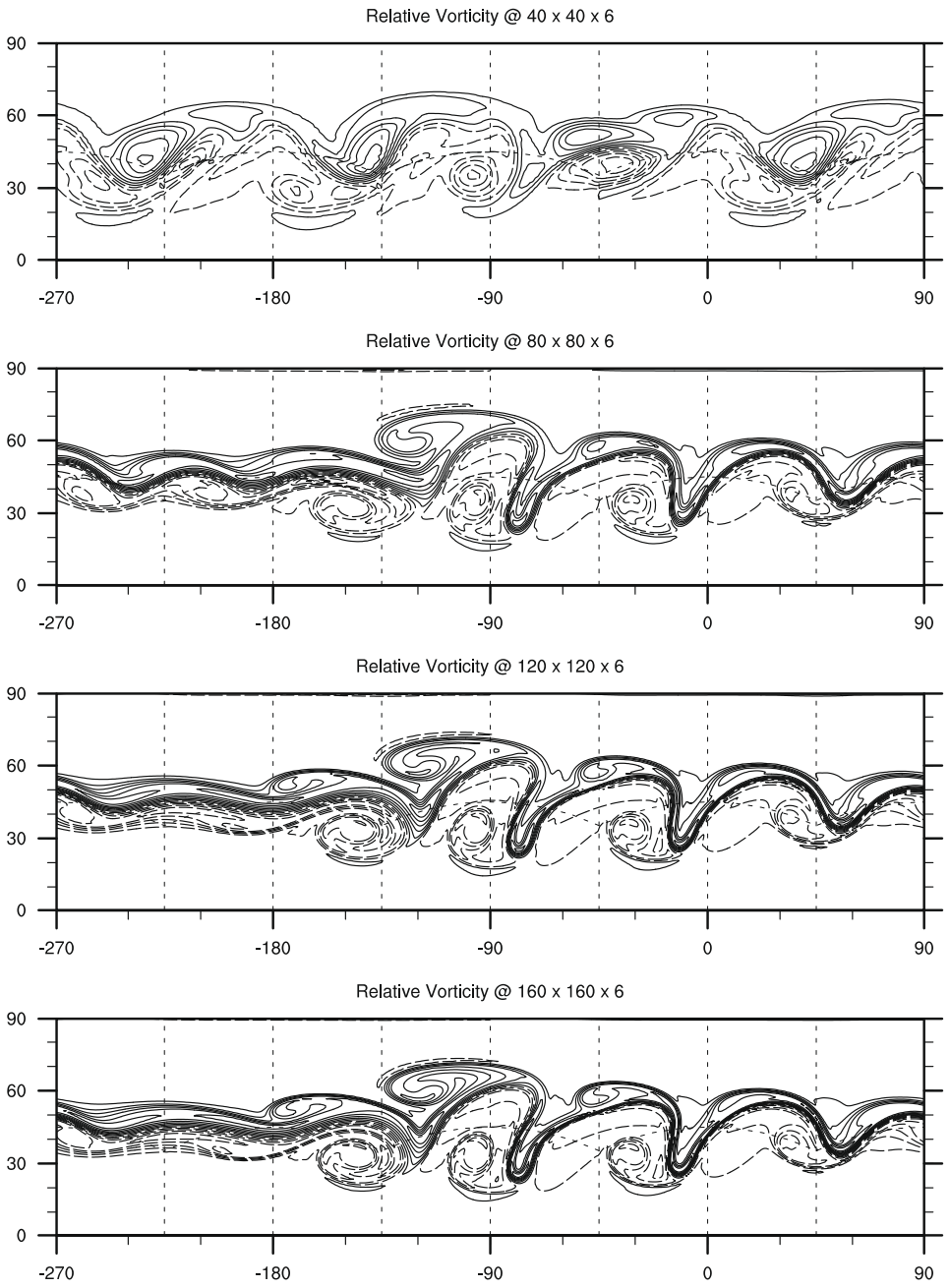

Fig. 19. Relative vorticity field associated with the barotropic instability test at day 6 obtained from the FV3s scheme with AUSM$^+$-up solver on a $40 \times 40 \times 6$ mesh (top), $80 \times 80 \times 6$ mesh (2nd from top), $120 \times 120 \times 6$ mesh (3rd from top) and $160 \times 160 \times 6$ mesh (bottom). Contour lines are in increments of $2.0 \times 10^{-5}\,s^{-1}$ from $-1.1 \times 10^{-4}\,s^{-1}$ to $-0.1 \times 10^{-4}\,s^{-1}$ (dashed) and from $0.1 \times 10^{-4}\,s^{-1}$ to $1.5 \times 10^{-4}\,s^{-1}$ (solid). The zero line is omitted. Only the northern hemisphere is depicted in this plot.

resolutions however, we observe convergence to the reference solution given by Galewsky et al. [12] and similarity to the solution calculated by Rossmanith [33] (except without the need to split the geostrophically balanced and unsteady modes).

7.7. Computational performance

The utility of any computational scheme is a function of both accuracy and computational performance. Hence, we present the relative cost of the third- and fourth-order schemes (along with each choice of Riemann solver) in Table 7. As expected, we see an overall increase in cost with increasing complexity of the Riemann solver, as well as a much more

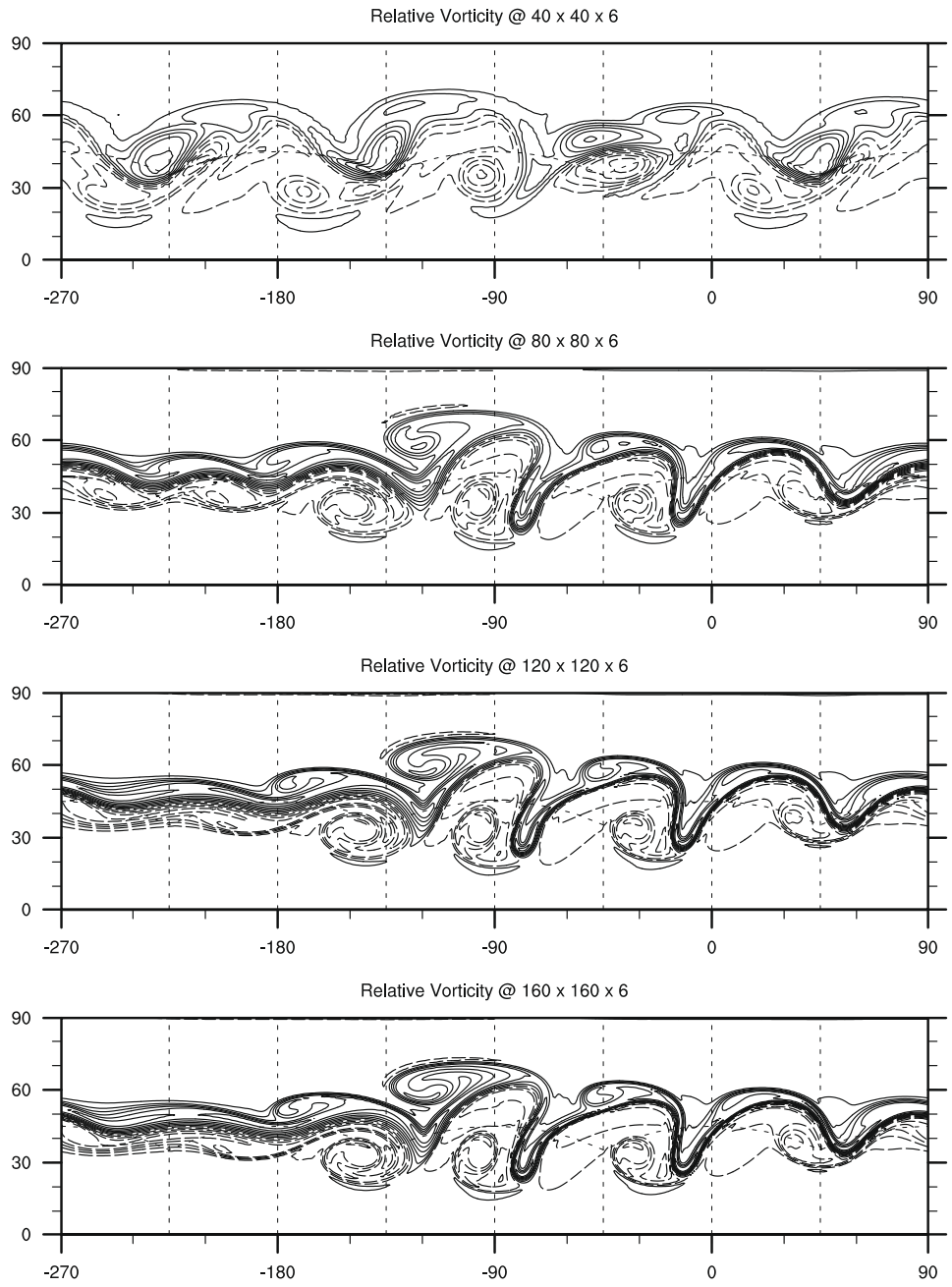

Fig. 20. As Fig. 19 except for the FV4 scheme.

Table 7
The approximate computational performance for each of the numerical schemes paired with each Riemann solver, as obtained from serial runs on a MacBook Pro with 2.4 GHz Intel Core 2 Duo. The timings correspond to the number of seconds required to simulate one day of Williamson test case 2 (described in Section 7.2) on a $40 \times 40 \times 6$ grid. A CFL number of 1.0 is used in all cases.

Scheme	Rusanov	Roe	AUSM$^+$-up
FV3s (s)	10.0	10.6	10.9
FV4 (s)	23.8	24.5	25.0

significant jump in computational cost associated with going from the third- to fourth-order scheme. As is usual for explicit methods, a doubling of the resolution will lead to an eight times increase in the computational time for the scheme when keeping the CFL number constant.

Considering the significant improvement in accuracy we have observed from using the Roe or AUSM$^+$-up Riemann solvers, the added expense they incur in computation time is negligible.

8. Conclusions and future work

In this paper, we have successfully demonstrated both a dimension-split piecewise-parabolic scheme and a fourth-order accurate piecewise-cubic method for solving the shallow-water equations on the sphere. We have applied both of these schemes to a set of test problems in order to verify accuracy, stability and convergence, including the shallow-water test cases of Williamson et al. [46] and the barotropic instability of Galewsky et al. [12]. Third- and fourth-order accuracy of these schemes is apparent in the smooth simulations tested in this paper.

Three Riemann solvers have been considered in this analysis, including the Rusanov numerical flux, the Roe solver of [31], and the AUSM$^+$-up numerical flux of Liou [23]. Our simulations have shown that the AUSM$^+$-up flux provides the best overall accuracy when applied to various shallow-water test cases, followed very closely by the Roe flux. The Rusanov solver has demonstrated significantly worse performance in terms of accuracy and conservation of flow invariants, which we believe outweighs its simplicity. Importantly, the overall improvement in accuracy due to the Roe or AUSM$^+$-up solvers has been shown to come without a significant added computational expense.

Extension of the work described herein to a full 3D atmospheric model certainly deserves some attention. Adaption of the Riemann solvers to the full Euler equations is a trivial task, but one must be careful in the reconstruction step and in making a choice of the timestepping method. The choice of reconstruction is dependent on the vertical coordinate system, of which there are three possible routes forward: First, the high-order FV approach discussed herein is perhaps most directly applied with a semi-Lagrangian vertical coordinate, such as that described by Lin [21]. Second, a static terrain-following coordinate could be adopted (see, for instance, [18,28,48]). Finally, a static height-based coordinate could be used, with topography incorporated via partial-shaved cells (see, for example, [1,7]). For the first two choices of vertical coordinate, it is unknown what effect the vertically non-Cartesian geometry will have on the accuracy of the reconstruction step. Analysis of these approaches represents ongoing research. The second two choices of vertical coordinate also introduce issues with regard to the choice of a vertical timestepping scheme, since atmospheric models must incorporate horizontal/vertical aspect ratios that are sometimes on the order of $\sim 10^3$. In this case, the vertical CFL condition tends to be unmanageably restrictive. To overcome this problem, one could either use a modified equation set that removes vertically-propagating soundwaves (see, for example, [3,11]) or use a dimension-split implicit–explicit integrator (such as the IMEX-RK scheme of Ascher et al. [4]). Other methods include semi-implicit treatment of sound waves or a split-explicit approach with subcycling. Research is ongoing as to the best route forward.

Acknowledgements

The authors thank Dr. Meng-Sing Liou for his assistance with fine-tuning the AUSM$^+$-up solver for unstable shallow-water flow and Dr. Smadar Karni for her assistance with the topography parameterization. This work was supported by the NSF Collaboration in Mathematical Geosciences (CMG) Grant ATM-0723440.

Appendix A. Treatment of panel boundaries

In this appendix we give a detailed description of the high-order boundary reconstruction process we apply at panel edges. For sake of brevity, we will focus on the third-order reconstruction, but note that a fourth-order reconstruction can be easily obtained using a similar method. The basic steps in our reconstruction process are summarized in Fig. A.21.

The first step in the treatment of panel boundaries requires a reconstruction of the form (44) to be built on the source panel. For the third-order boundary reconstruction we make use of minimal 3×3 stencils so as to obtain a piecewise-parabolic reconstruction. Increasing the accuracy of the boundary reconstruction via larger stencils or a higher-order reconstruction will generally lead to an increase in the model's global accuracy, but the effect on the overall accuracy of the scheme is generally minor. Since information in ghost regions is not known, elements that are immediately adjacent to panel edges must approximate derivatives perpendicular to the panel edge using one-sided stencils. One such set of stencils used for these reconstructions are depicted in Fig. A.22.

In Fig. A.22(a) and (c), we make use of one-sided reconstructions for the first and second derivatives in the α direction,

$$\left(\frac{\delta q}{\delta \alpha}\right)_i = \frac{-3\bar{q}_i + 4\bar{q}_{i+1} - \bar{q}_{i+2}}{2\Delta\alpha} + O(\Delta\alpha^2, \Delta\beta^2), \tag{A.1}$$

$$\left(\frac{\delta^2 q}{\delta \alpha^2}\right)_i = \frac{\bar{q}_i - 2\bar{q}_{i+1} + \bar{q}_{i+2}}{\Delta\alpha^2} + O(\Delta\alpha, \Delta\beta^2). \tag{A.2}$$

In (c) these one-sided approximations must also be utilized for derivatives in the β direction. Cross-derivatives are approximated in reconstruction (a) via

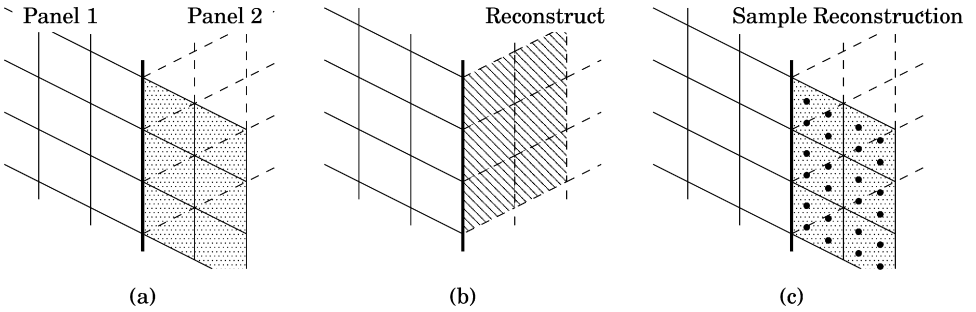

Fig. A.21. (a) Reconstruction at panel boundaries is necessitated by the fact that the ghost-elements of one panel (Panel 1) do not correspond exactly to elements on a neighboring panel (Panel 2) where element-averages are known exactly. (b) The first step in reconstruction requires one-sided derivative approximations to be calculated on Panel 2 so as to develop a sub-grid-scale reconstruction of the form (44). (c) The one-sided reconstructions are then sampled over four Gauss points (per element on Panel 1) so as to ensure high-order accuracy.

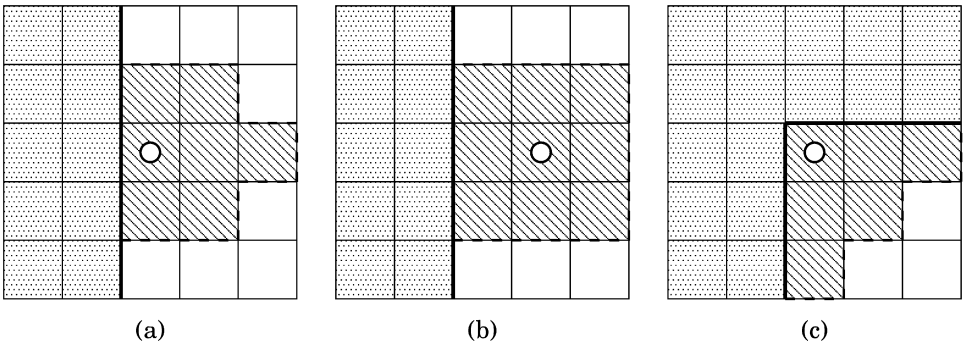

Fig. A.22. A set of one-sided stencils for the third-order boundary reconstruction along the left edge. Shading indicates ghost-elements, where information is unavailable. Elements used for computing a reconstruction in the specified element are shown with diagonal hatching. Reconstructions along other panel edges can be obtained via a straightforward rotation of the given stencils.

$$\left(\frac{\delta^2 q}{\delta\alpha\delta\beta}\right)_{i,j} = \frac{\bar{q}_{i+1,j+1} - \bar{q}_{i,j+1} - \bar{q}_{i,j-1} + \bar{q}_{i,j-1}}{2\Delta\alpha\Delta\beta} + O(\Delta\alpha, \Delta\beta^2), \tag{A.3}$$

and in (c) by

$$\left(\frac{\delta^2 q}{\delta\alpha\delta\beta}\right)_{i,j} = \frac{\bar{q}_{i+1,j} - \bar{q}_{i,j} - \bar{q}_{i+1,j-1} + \bar{q}_{i,j-1}}{\Delta\alpha\Delta\beta} + O(\Delta\alpha, \Delta\beta). \tag{A.4}$$

Note that in Fig. A.22(b) we may utilize standard central reconstructions on a 3×3 stencil to approximate all derivatives.

Once the one-sided reconstruction is established, we can sample each ghost element on the source grid using four-point Gaussian quadrature so as to obtain element-averages on the destination grid. Since the reconstruction obtained in the first step is at least third-order accurate, the reconstructed element-averages in each ghost cell will also be third-order accurate.

The process described in this section must be applied whenever boundary information is needed from an adjacent panel. Hence, under a RK3 timestepping scheme, this process must be applied three times per timestep.

References

[1] A. Adcroft, C. Hill, J. Marshall, Representation of topography by shaved cells in a height coordinate ocean model, Mon. Weather Rev. 125 (1997) 2293.
[2] F. Alcrudo, P. Garcia-Navarro, A high-resolution Godunov-type scheme in finite volumes for the 2D shallow-water equations, Int. J. Numer. Methods Fluids 16 (1993) 489–505.
[3] A. Arakawa, C.S. Konor, Unification of the anelastic and quasi-hydrostatic systems of equations, Mon. Weather Rev. 137 (2009) 710–726.
[4] U.M. Ascher, S.J. Ruuth, R.J. Spiteri, Implicit–explicit Runge–Kutta methods for time-dependent partial differential equations, Appl. Numer. Math. 25 (1997) 151–167.
[5] D.S. Bale, Wave propagation algorithms on curved manifolds with applications to relativistic hydrodynamics, Ph.D. Thesis, University of Washington, 2002.
[6] M. Barad, P. Colella, A fourth-order accurate local refinement method for Poisson's equation, J. Comput. Phys. 209 (2005) 1–18.
[7] T.L. Black, The new NMC mesoscale eta model: description and forecast examples, Weather Forecast. 9 (1994) 265–284.
[8] C. Chen, F. Xiao, Shallow water model on cubed-sphere by multi-moment finite volume method, J. Comput. Phys. 227 (2008) 5019–5044.

[9] P. Colella, P.R. Woodward, The piecewise parabolic method (PPM) for gas-dynamical simulations, J. Comput. Phys. 54 (1984) 174–201.
[10] J. Côté, A. Staniforth, An accurate and efficient finite-element global model of the shallow-water equations, Mon. Weather Rev. 118 (1990) 2707–2717.
[11] T. Davies, A. Staniforth, N. Wood, J. Thuburn, Validity of anelastic and other equation sets as inferred from normal-mode analysis, Quart. J. Roy. Meteorol. Soc. 129 (2003) 2761–2775.
[12] J. Galewsky, R.K. Scott, L.M. Polvani, An initial-value problem for testing numerical models of the global shallow-water equations, Tellus Series A 56 (2004) 429–440.
[13] F.X. Giraldo, J.S. Hesthaven, T. Wartburton, Nodal high-order discontinuous Galerkin methods for the shallow water equations, J. Comput. Phys. 181 (2002) 499–525.
[14] S. Gottlieb, C.-W. Shu, E. Tadmor, Strong stability-preserving high-order time discretization methods, SIAM Rev. 43 (1) (2001) 89–112.
[15] H. Guillard, C. Viozat, On the behaviour of upwind schemes in the low Mach number limit, Comput. Fluids (1999) 63–86.
[16] R. Heikes, D.A. Randall, Numerical integration of the shallow water equations on a twisted icosahedral grid. Part I: Basic design and results of tests, Mon. Weather Rev. 123 (1995) 1862–1880.
[17] R. Jakob-Chien, J.J. Hack, D.L. Williamson, Spectral transform solutions to the shallow water test set, J. Comput. Phys. 119 (1995) 164–187.
[18] A. Kasahara, Various vertical coordinate systems used for numerical weather prediction, Mon. Weather Rev. 102 (1974) 509.
[19] P.D. Lax, Weak solutions of non-linear hyperbolic equations and their numerical computation, Commun. Pure Appl. Math. VII (1954) 159–193.
[20] R. LeVeque, Wave propagation algorithms for multidimensional hyperbolic systems, J. Comput. Phys. 131 (1997) 327–353.
[21] S. Lin, A "vertically lagrangian" finite-volume dynamical core for global models, Mon. Weather Rev. 132 (2004) 2293–2307.
[22] S.-J. Lin, R.B. Rood, An explicit flux-form semi-Lagrangian shallow water model on the sphere, Quart. J. Roy. Meteorol. Soc. 123 (1997) 2477–2498.
[23] M.-S. Liou, A sequel to AUSM. Part II: AUSM+-up for all speeds, J. Comput. Phys. 214 (2006) 137–170.
[24] M.-S. Liou, C. Steffen, A new flux splitting scheme, J. Comput. Phys. 107 (1993) 23–39.
[25] Y. Liu, C. Shu, E. Tadmor, M. Zhang, Central discontinuous Galerkin methods on overlapping cells with a non-oscillatory hierarchical reconstruction, SIAM J. Numer. Anal. 45 (2007) 2442–2467.
[26] R.D. Nair, S.J. Thomas, R.D. Loft, A discontinuous Galerkin global shallow water model, Mon. Weather Rev. 133 (2005) 876–888.
[27] S. Noelle, N. Pankratz, G. Puppo, J.R. Natvig, Well-balanced finite volume schemes of arbitrary order of accuracy for shallow water flows, J. Comput. Phys. 213 (2006) 474–499.
[28] N.A. Phillips, A coordinate system having some special advantages for numerical forecasting, J. Atmos. Sci. 14 (1957) 184–185.
[29] W.M. Putman, S.-J. Lin, Finite-volume transport on various cubed-sphere grids, J. Comput. Phys. 227 (2007) 55–78.
[30] W.M. Putman, S.-J. Lin, A finite-volume dynamical core on the cubed-sphere grid, in: N.V. Pogorelov, E. Audit, P. Colella, G.P. Zank (Eds.), Numerical Modeling of Space Plasma Flows: Astronum-2008, vol. 406, Astronomical Society of the Pacific Conference Series, 2009, pp. 268–276.
[31] P.L. Roe, Approximate Riemann solvers, parameter vectors, and difference schemes, J. Comput. Phys. 43 (1981) 357–372.
[32] C. Ronchi, R. Iacono, P.S. Paolucci, The "cubed-sphere": A new method for the solution of partial differential equations in spherical geometry, J. Comput. Phys. 124 (1) (1996) 93–114.
[33] J.A. Rossmanith, A wave propagation method for hyperbolic systems on the sphere, J. Comput. Phys. 213 (2006) 629–658.
[34] V.V. Rusanov, Calculation of intersection of non-steady shock waves with obstacles, J. Comput. Math. Phys. USSR 1 (1961) 267–279.
[35] R. Sadourny, Conservative finite-difference approximations of the primitive equations on quasi-uniform spherical grids, Mon. Weather Rev. 100 (1972) 136–144.
[36] A. St-Cyr, C. Jablonowski, J.M. Dennis, H.M. Tufo, S.J. Thomas, A comparison of two shallow-water models with nonconforming adaptive grids, Mon. Weather Rev. 136 (2008) 1898–1922.
[37] M. Taylor, J. Tribbia, M. Iskandarani, The spectral element method for the shallow water equations on the sphere, J. Comput. Phys. 130 (1997) 92–108.
[38] M.A. Taylor, J. Edwards, A. St.Cyr, Petascale atmospheric models for the community climate system model: new developments and evaluation of scalable dynamical cores, J. Phys. Conf. Ser. 125 (2008) 012023.
[39] S.J. Thomas, R.D. Loft, The NCAR spectral element climate dynamical core: semi-implicit Eulerian formulation, J. Sci. Comput. 25 (1) (2005) 307–322.
[40] J. Thuburn, Y. Li, Numerical simulations of Rossby Haurwitz waves, Tellus Series A 52 (2000) 181–189.
[41] H. Tomita, M. Tsugawa, M. Satoh, K. Goto, Shallow water model on a modified icosahedral geodesic grid by using spring dynamics, J. Comput. Phys. 174 (2001) 579–613.
[42] E.F. Toro, Riemann Solvers and Numerical Methods for Fluid Dynamics, second ed., Springer, 1999. ISBN-10: 3540659668, 624 pp.
[43] P.A. Ullrich, P.H. Lauritzen, C. Jablonowski, Geometrically exact conservative remapping (GECoRe): regular latitude–longitude and cubed-sphere grids, Mon. Weather Rev. 137 (2009) 1721–1741.
[44] B. Van Leer, Towards the ultimate conservative difference scheme. V – A second-order sequel to Godunov's method, J. Comput. Phys. 32 (1979) 101–136.
[45] B. Van Leer, J. Thomas, P. Roe, R. Newsome, A Comparison of Numerical Flux Formulas for the Euler and Navier–Stokes Equations, AIAA Paper No. 87-1104-CP, 1987.
[46] D. Williamson, J. Drake, J. Hack, R. Jakob, P. Swarztrauber, A standard test set for numerical approximations to the shallow water equations in spherical geometry, J. Comput. Phys. 102 (1992) 211–224.
[47] D.L. Williamson, Equivalent finite volume and Eulerian spectral transform horizontal resolutions established from aqua-planet simulations, Tellus Series A 60 (2008) 839–847.
[48] N. Wood, A. Staniforth, The deep-atmosphere Euler equations with a mass-based vertical coordinate, Quart. J. Roy. Meteorol. Soc. 129 (2003) 1289–1300.
[49] S.T. Zalesak, Fully multidimensional flux-corrected transport algorithms for fluids, J. Comput. Phys. 31 (1979) 335–362.